BSGF - Earth Sciences Bulletin 2022, 193, 12
© D. Lévy *et al.*, Published by EDP Sciences 2022
https://doi.org/10.1051/bsgf/2022015

BSGF
Earth Sciences Bulletin
Available online at:
www.bsgf.fr

Open Access

Successive phases of serpentinization and carbonation recorded in the Sivas ophiolite (Turkey), from oceanic crust accretion to post-obduction alteration

Dan Lévy[1,*], Jean-Paul Callot[1], Isabelle Moretti[1,2], Mathieu Duttine[3], Brigitte Dubreuil[4], Philippe de Parseval[5] and Omar Boudouma[2]

[1] LFCR – Laboratoire des Fluides Complexes et leurs Réservoirs, E2S UPPA – Université de Pau et des Pays de l'Adour, CNRS, Total, Pau, France
[2] ISTeP – Institut des Sciences de la Terre de Paris, Université Pierre et Marie Curie, Paris, France
[3] ICMCB – Institut de Chimie de la Matière Condensée de Bordeaux, Bordeaux, France
[4] LCA – Laboratoire de Chimie Agro-industrielle, Université de Toulouse, INRAE, Toulouse, France
[5] GET – Géosciences Environnement Toulouse, Université de Toulouse, UPS, CNRS, IRD, Toulouse, France

Received: 10 February 2022 / Accepted: 20 July 2022 / Publishing online: 12 August 2022

Abstract – The ophiolite of Sivas (Turkey) was studied in order to define the chronology of different alteration events related to a series of serpentinization and carbonation episodes. Six samples were investigated, representative of different types of ophicalcite (partially carbonated serpentinite). X-ray diffraction (XRD) and Mössbauer spectroscopy were used to determine the bulk mineralogy and the bulk Fe^{3+}/Fe_{tot} ratio, respectively. Electron microprobe and secondary ion mass spectrometer (SIMS) analyses were also conducted to identify the chemical composition of different mineral phases in addition to the carbon and oxygen isotopic compositions of calcite. An initial, *i.e.* pre-obduction, phase of olivine and pyroxene serpentinization was followed by a brecciation event associated with precipitation of massive serpentine. This first alteration event occurred during exhumation of the peridotites to the seafloor, followed by a carbonation event at temperatures in the range 35−100 °C. A low-temperature (~35 °C) carbonation event occurred between 90 and 65 Ma. Finally, a reheating of the system likely occurred after the obduction at 55−40 Ma, resulting in a carbonation episode followed by late serpentinization. Our study presents the first direct evidence of serpentinization after obduction. In that geological context, the hydrogen produced during the proposed multiphase serpentinization may have been trapped by the salt deposits overlying the ophiolite but subsurface data will be necessary to define potential traps and reservoirs; further studies are also needed to determine whether the serpentinization process is still ongoing.

Keywords: Sivas / ophiolite / ophicalcite / serpentinization / carbonation / H_2

Résumé – Multiples épisodes de serpentinisation et de carbonatation enregistrés par l'ophiolite de Sivas (Turquie), de la zone d'accrétion de croûte océanique à l'altération tardive post-obduction. L'ophiolite de Sivas (Turquie) a été étudiée pour caractériser les différents épisodes de serpentinisation et de carbonatation. Pour cela, six échantillons représentatifs des différents types d'ophicalcite (serpentinite partiellement carbonatée) ont été analysés. La diffraction des rayons X et la spectroscopie Mössbauer ont été utilisées pour déterminer respectivement la minéralogie et le rapport Fe^{3+}/Fe_{tot} en roche totale. Les analyses en microsonde électronique et au spectromètre de masse à ions secondaires ont permis d'identifier la composition chimique des différentes phases et la signature isotopique en carbone et en oxygène des calcites. Ces mesures ont permis de proposer un modèle où l'olivine et le pyroxène ont été serpentinisés avant de subir une bréchification menant à la précipitation de serpentine massive dans les fractures. Ce premier épisode d'altération a eu lieu durant l'exhumation des péridotites, suivie par une carbonatation entre 35 °C et 100 °C. Une autre carbonatation basse température (~35 °C) a ensuite eu lieu entre 90 et 65 Ma. Enfin, un réchauffement du système a probablement eu lieu après obduction entre 55 et 40 Ma menant à une carbonatation et une serpentinisation tardive. C'est ainsi la première évidence directe de serpentinisation

*Corresponding author: dlevy001@univ-pau.fr

post-obduction. Il n'est pas clair si l'hydrogène produit durant les différents épisodes de serpentinisation a été piégé par les dépôts de sel sus-jacents et d'autres études seront nécessaires pour comprendre si la serpentinisation est toujours en cours.

Mots clés : Sivas / ophiolite / ophicalcite / serpentinisation / carbonatation / H_2

1 Introduction

Ophiolites are fragments of oceanic lithosphere that have been thrusted onto the continental margin. The oceanic crusts and lithospheres are commonly altered by seawater at the mid-ocean ridge (MOR) during exhumation and emplacement of mantle rock at sea bed, and by meteoric and basinal fluids when they outcrop after shortening event and induced thrusting. This alteration often leads to partial to complete serpentinization of the ophiolitic peridotite. This serpentinization is coupled with the production of dihydrogen (H_2) by the redox reaction between H_2O and Fe^{2+}:

$$2FeO + H_2O \rightarrow Fe_2O_3 + H_2, \quad (1)$$

where ferrous iron can come from the olivine or pyroxene and ferric iron be formed in magnetite and can even be present in serpentine. The serpentinization occurs both at the seafloor (Charlou *et al.*, 2002) and at the surface of continents (Combaudon *et al.*, 2022; Vacquand *et al.*, 2018). Fe^{2+} can be present in primary minerals of unaltered peridotites (*e.g.*, olivine ($(Mg,Fe)_2SiO_4$) and pyroxene ($(Mg,Fe)_2Si_2O_6$) and secondary minerals of altered peridotites (*e.g.*, Fe-brucite ($(Mg,Fe)(OH)_2$), serpentine ($(Mg,Fe)_3Si_2O_5(OH)_4$) and magnetite (Fe_3O_4): Bach *et al.*, 2006; D'Antonio and Kristensen, 2004; Frost *et al.*, 2013; Moody, 1976; Seyfried *et al.*, 2007). Therefore, petrological investigation of partially to completely serpentinized peridotite may provide crucial insight regarding its H_2 generation potential, both in the past and at present. Such petrological investigation, combined with isotopic analyses, could help to better distinguish whether there is continuous H_2 outflow from the seafloor to the continent, or sporadic H_2 production within each serpentinization episode.

This study focuses on the Late Cretaceous ophiolite from Sivas in Turkey. This ophiolite sequence forms the basement of the Tertiary Sivas Basin, which is characterized by intense salt tectonic activity (*e.g.* Legeay *et al.*, 2019). The basin constitutes a vertical sequence of ophiolite where several episodes of serpentinization are evident and commonly followed by carbonation. The purpose of this study is to quantify the alteration episodes and constrain their chronology. Although H_2 seeps are present in the nearby Tekirova ophiolite (*i.e.*, the Chimaera seep: Etiope *et al.*, 2011; Hosgormez *et al.*, 2008), no evidence of H_2 seeps has been found related to the Sivas ophiolite. Considering the thickness of the evaporites overlying the ophiolite, a geological trap of H_2 may be possible, questioning the presence of this green resource (Moretti, 2019), unless the faults here allow gas migration to the surface. Additionally, the geological history of the Sivas ophiolite is quite similar to that of the Samail ophiolite in Oman, where H_2 production results from hyperalkaline springs in a way similar to what is observed in the ophiolites in the Philippines, New Caledonia, Turkey, Italy, Canada (Abrajano *et al.*, 1990; Abrajano *et al.*, 1988; Barnes *et al.*, 1967; Bruni *et al.*, 2002; Cardace *et al.*, 2015; Chavagnac *et al.*, 2013; Cipolli *et al.*, 2004; Deville and Prinzhofer, 2016; Deville *et al.*, 2010; Etiope *et al.*, 2013; Meyer-Dombard *et al.*, 2015; Neal and Stanger, 1983; Sano *et al.*, 1993; Szponar *et al.*, 2013; Woycheese *et al.*, 2015). Although such springs have not been observed in relation to the Sivas ophiolite, it is necessary to study the serpentinites with an emphasis on their H_2 potential, in order to compare them with other ophiolites in Turkey and Oman.

Here, we present a detailed petrological, textural, and geochemical study of different types of ophicalcite (partially carbonated serpentinite) in the Sivas ophiolite. The aim is to reconstruct the chronology of different serpentinizing and carbonating fluid flow events and constrain their chemical conditions, temperatures, and oxygen fugacities (fO_2).

2 Geological setting

Central Anatolia consists of three crustal Blocks (the Pontides, Kırsehir, and Tauride Blocks that are delimited by suture zones that contain ophiolites. In western Anatolia, the Pontides and Tauride–Anatolide Blocks are delimited by the İzmir–Ankara–Erzincan Suture Zone (IAESZ), which marks the Late Cretaceous to Early Paleogene closure of the northern branch of the Neo-Tethys. The Tauride Block is delimited to the south by the Cyprus Suture Zone, which represents a remnant of the southern Neo-Tethys branch. The Kırsehir Block (Legeay *et al.*, 2019) crosscuts the oceanic lithosphere after regional burial, as indicated by relicts of ophiolitic mélange and obducted suprasubduction-zone ophiolite fragments (Lefebvre *et al.*, 2011; Legeay *et al.*, 2019; van Hinsbergen *et al.*, 2016; Yaliniz *et al.*, 2000). The ophiolite was obducted between the late Santonian and pre-late Campanian. It is covered by sedimentary successions consisting of Maastrichtian to Thanetian shallow-water platform carbonates (Tecer Formation: İnan and İnan, 1990; Legeay *et al.*, 2019), changing northward to middle Eocene transgressive marine facies of the Çerpaçindere Formation (Aktïmur *et al.*, 1990). The late Eocene "Bartonian" regressive phase resulted in deposition of the Tuzhisar evaporite (Pichat, 2017; Pichat *et al.*, 2021). A first generation of continental mini-basins were formed and subsequently infilled by sediments of the Selimiye Formation. A second generation of mini-basins followed during the Oligocene, separated from the primary mini-basins by the evaporite canopy. A transgression followed during the early Miocene (Callot *et al.*, 2014; Kergaravat *et al.*, 2017; Kergaravat *et al.*, 2016; Legeay, 2017; Pichat, 2017; Pichat *et al.*, 2018; Ribes, 2015; Ribes *et al.*, 2018; Ribes *et al.*, 2015; Ringenbach et al., 2013).

The Sivas ophiolite crops out along the southern boundary of the Sivas Basin and extends for over 100 km from west to east and for a few kilometers from north to south. The study area lies between the Gürlevik/Tecer Mountains to the north

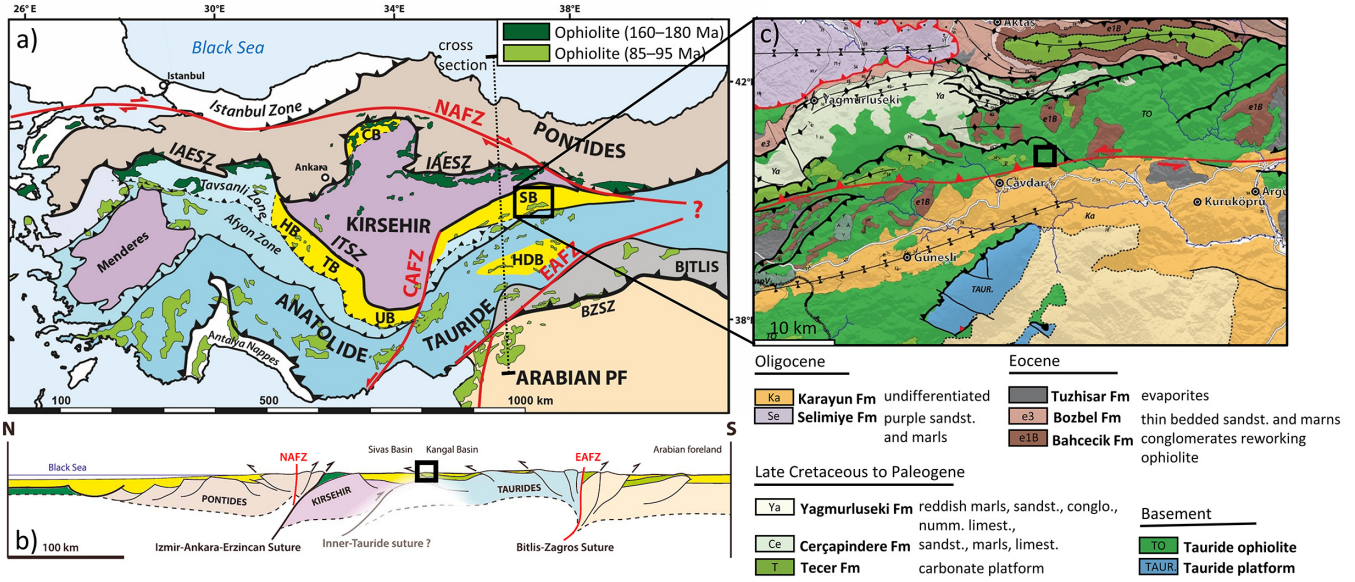

Fig. 1. (a) A tectonic map of Turkey and the Eastern Mediterranean region illustrating major suture zones, faults systems, ophiolite outcrops, and tectonic units (Legeay *et al.*, 2019). (b) N–S cross-section showing the relationship between crustal blocks and ophiolites (Legeay *et al.*, 2019). (c) A geological map of the Sivas Basin with the sampling zone indicated by a yellow point. The location of the sampling zone is illustrated by a black square (b, c). conglo.: conglomerate; limest.: limestone; numm.: nummulitic; sandst.: sandstone.

and the Tauride carbonate platform to the south (Fig. 1). From seismic data, it has been determined that the ophiolite is located at the bottom of the foreland basin and involved in the thrust slices (Legeay *et al.*, 2019).

The pre-obduction evolution of the oceanic domain north of the future Sivas Basin shows that the Sivas ophiolite is characterized by serpentinized peridotites (mostly harzburgite), with minor magmatic intrusions and chromite pods (Legeay *et al.*, 2019). The top of the serpentinized mantle is characterized by cataclastic deformation with several phases of ophicalcite, which are interpreted as an extensional detachment fault (Legeay *et al.*, 2019). Based on two samples from the rare magmatic intrusions, U–Pb zircon dating yielded approximate ages of 91.49 ± 0.8 Ma and 72.7 ± 0.5 Ma. Petrological and geochemical data also revealed that the magmatic intrusions were affected by hydrothermal metasomatism early after the emplacement of oceanic crust. These data highlight that the Sivas ophiolite may have recorded forearc hyperextension in the context of the Late Cretaceous suprasubduction zone. Post-obduction evolution is characterized by the deposition of a Maastrichtian–Paleocene carbonate platform (Tecer and Gürlevik platforms) overlying the ophiolite, followed by clastic sediments containing reworked ophiolitic and Mesozoic Tauride clasts.

3 Methods

3.1 Sampling

Increased proximity to the Tecer carbonate ridges enhances the carbonation of the serpentinites, leading to breccias with clasts of serpentine surrounded by a carbonated matrix (Fig. 2). The term ophicalcite can therefore be used to describe these samples (Lemoine *et al.*, 1987; Artemyev and Zaykov, 2010). We refer here to three types of ophicalcite corresponding to the six rocks that were sampled:

- type I (Fig. 2b, c) describes serpentinites crosscut by large veins of calcite. We distinguish type Ia deposits with veins of calcite (A1*) from type Ib deposits containing veins of massive serpentinite partially replaced by calcite (B1–2*);
- type II (Fig. 2d) describes monogenic breccia with serpentinite clasts surrounded by calcite (C1*) and more or less residual serpentine (D1*);
- type III (Fig. 2e) describes polygenic breccias with different clasts from the ophiolite (serpentinite, amphibolite, chromitite) surrounded by calcite (E1*).

3.2 Petrographic inspection

3.2.1 Optical microscopy

Thin sections (30 μm thick) were prepared for the collected samples in order to undertake petrographic study at the microscopic scale. We used a Nikon Eclipse LV100ND microscope to investigate the thin sections. We also performed cathodoluminescence analysis to study calcite cements and fracture infill, using a Nikon Labophot-2 microscope combined with a cathodyne (12–20 kV and 200–400 mA).

3.2.2 Raman microspectroscopy

The different phases of serpentine (chrysotile, lizardite, antigorite) were distinguished using Raman microspectroscopy (performed with the instruments of the Equipex-CRITEX at the LCA, Toulouse-INP). We used a LabRAM HR evolution spectrometer (HORIBA Jobin Yvon Ltd), equipped with a grating (600 grooves/mm) and combined with an Olympus microscope with a 532 nm laser. A long-working-distance objective lens (50×) provided a 1.3 μm focal spot size. The measurements were performed with a power of 12.5 mW for two spectral ranges: 100–1200 cm^{-1} and 3600–3750 cm^{-1}. First, punctual analyses were made with

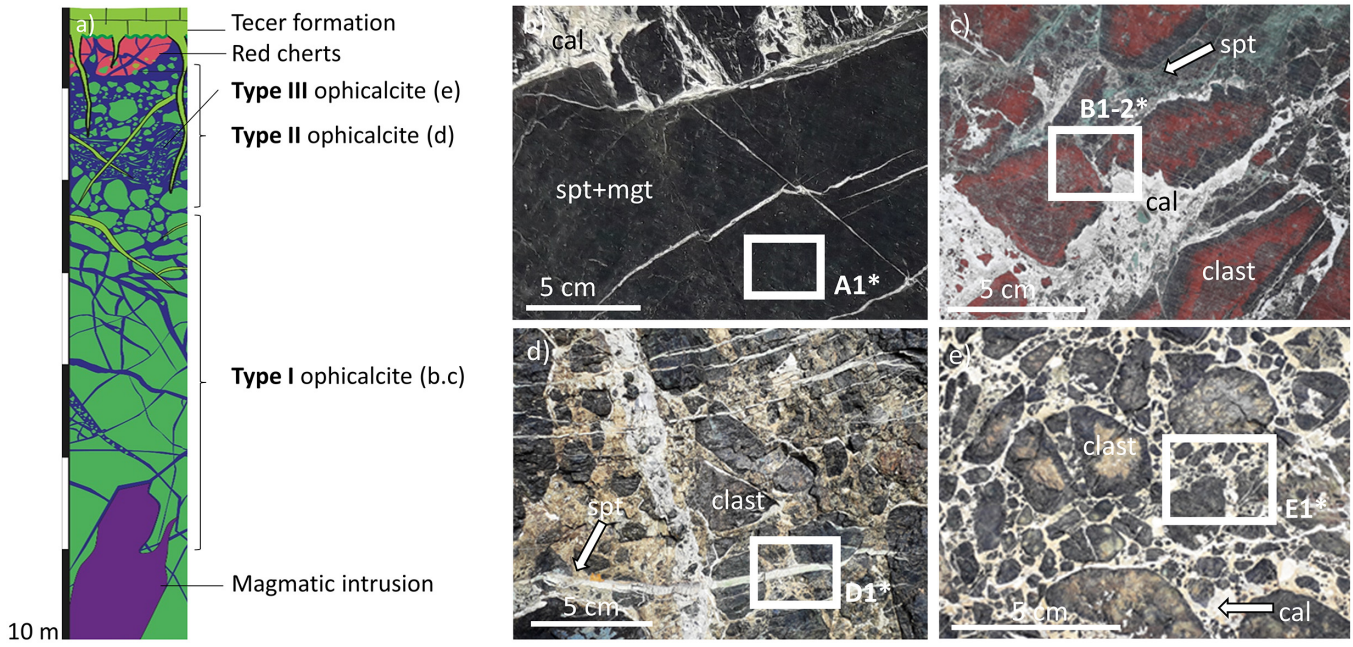

Fig. 2. (a) Illustrative vertical profile of the ophiolite (modified from Legeay *et al.*, 2019). (b, c) Type I ophicalcite constituting serpentinite clasts several decimeters in size, taken in massive serpentine with different degrees of carbonation. (d) Type II ophicalcite with serpentinite clasts surrounded by a matrix of calcite and serpentine. (e) Type III ophicalcite containing different rounded clasts surrounded by calcite. cal: calcite; spt: serpentine.

an acquisition duration of 5 min distributed over two accumulations. The Raman spectrometer was calibrated with a silicon standard. Secondly, mapping was undertaken for the spectral range 3600−3750 cm^{-1} with a 0.4 s acquisition time, repeated during three accumulations. These parameters were based on measurements by Noël (2019).

3.2.3 X-ray diffraction

The rock samples were crushed by hand in an agate mortar and sieved to 100 μm for X-ray diffraction analyses using a D2 Phaser from Bruker (LFCR, Pau). The CuKα radiation at 30 kV and 10 mA and the SSD160 detector were used. Measurements were made with a step size of 0.02°, with a step time of 0.2 s/step in the range 5−80° (2θ) with 30 trs/min.

3.3 Chemical analyses

3.3.1 Electron microscopy

Electron microscopy was performed on thin sections coated with 20 nm carbon. The samples were imaged using scanning electron microscopy (SEM, Zeiss Supra 55VP, ISTeP, Paris) with an electron beam at 15 keV and an angular selective backscatter (AsB) detector. Some energy dispersive spectroscopy (EDS) maps were also acquired with this SEM to study oxide distribution and Fe zonation in serpentines.

3.3.2 Electron microprobe

Punctual quantitative chemical analyses were conducted using an electron microprobe (CAMECA SX-Five, Centre Raimond Castaing, Toulouse, France). We used a primary beam of 15 kV and 10 nA. The spot size was 2 μm for serpentine and 10 μm for calcite. The measured elements were Na, Si, Al, K, Mn, Fe, F, Mg, Cl, Cr, Ni (with Kα), and Ba (with Lα), with the respective standards albite, wollastonite, corundum, sanidine, pyrophanite, hematite, topaz, periclase, tugtupite, chromite, nickel metal, and barite. A qualitative map was also obtained with a step size of 4 μm, a dwell time of 0.2 s, and a primary beam at 15 kv and 20 nA. The measured elements were Si, Mg, Fe, Ca Cr, Na, Al, Mn, K, and Ti (with Kα).

3.3.3 Mössbauer spectroscopy

Zones of interest were crushed into an agate mortar to provide 500 mg of powder per analysis. The powder was then analyzed with a constant acceleration Halder-type spectrometer (ICMCB, Bordeaux) equipped with a ^{57}Co radioactive source (embedded in a Rh matrix) maintained at 293 K. The spectrometer was calibrated using a pure α-Fe^0 foil for external reference. All spectra were recorded in transmission geometry at ambient temperature. The Mössbauer hyperfine parameters and the relative areas of each component were refined using the WinNormos software (Wissenschaftliche Elektronik GmbH). Three analyses were made per zone, each analysis with a duration of ~3 days. The results are presented as the average of the three analyses with the associated error (2σ).

3.3.4 Stable isotope analyses

Carbon and oxygen isotopes of the calcite phases were measured by secondary ion mass spectrometry (SIMS) using a CAMECA IMS 1270 (CRPG, Nancy). A Cs^+ primary beam of

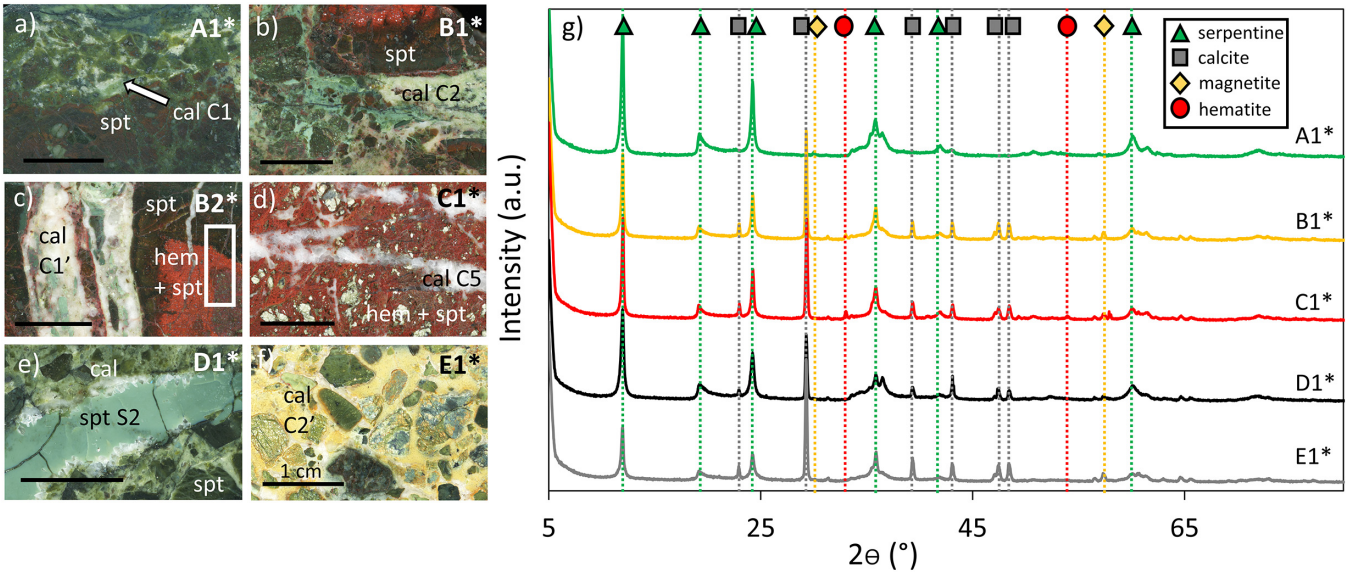

Fig. 3. Polished section of (a–d) type I (A1*, B1–2*, C1*), (e) type II (D1*), and (f) type III (E1*) ophicalcites with different degrees of hematitization. The rectangle zone in (d) represents the zone of interest in Figure 5. Scale bars indicate 1 cm. (g) XRD spectra of the different rocks. cal: calcite; hem: hematite; mgt: magnetite; spt: serpentine.

2 nA bombarded the samples for pre-sputtering for a duration of 90 s over an area of 25 μm^2. Measurements were then performed over 20 μm^2 during 40 cycles of 5 s each. Under these conditions, carbon isotopes were first measured in multicollection on a Faraday cup (FC) for ^{12}C and an electron multiplier for ^{13}C. Oxygen isotopes (^{16}O, ^{18}O) were then measured in multicollection on two FCs on a close spot. The measurements were performed on thin sections coated with 40 nm of Au. An in-house standard of calcite from CRPG was used.

The isotopic data are present under the $\delta^{13}C$ and $\delta^{18}O$ expressions, using PDB and SMOW standards respectively:

$$\delta^{13}C = \left(\frac{\left(\frac{^{13}C}{^{12}C}\right)_{sample}}{\left(\frac{^{13}C}{^{12}C}\right)_{standard}} - 1 \right) \times 1000,$$

$$\delta^{18}O = \left(\frac{\left(\frac{^{18}O}{^{16}O}\right)_{sample}}{\left(\frac{^{18}O}{^{16}O}\right)_{standard}} - 1 \right) \times 1000.$$

4 Results

4.1 Petrology

Based on XRD patterns, the dominant phases are serpentine and calcite in all investigated samples, except for sample A1*, where calcite was not detected (Fig. 3g). Magnetite (Fe_3O_4) was detected in every sample, whereas hematite (Fe_2O_3) was found to occur only in B2* and C1*. The presence and abundance of hematite can be assessed qualitatively in hand specimen, as indicated by the reddish color of samples B2* and C1*. Finally, we note that neither olivine nor pyroxene were detected, which suggests a high degree of serpentinization. The following sections provide detailed descriptions of the samples based on their ophicalcite group, from type I to type III.

4.1.1 Type I ophicalcite

Type I ophicalcites (A1*) display the lowest carbonate content. A typical pseudomorphic mesh texture can be observed (Fig. 4b, d), reflecting the replacement of primary olivine crystals by serpentine. The mesh corresponds to a microfracture network with different types of serpentine from the center to the outer part more or less associated to magnetite. Pyroxene crystals have also been replaced by serpentine, which we hereafter term "bastite" in order to distinguish it from the replacement of olivine. The cores of the mesh range in size (50−100 μm). Bastite crystals are larger (500 μm to 1 mm) and clearly seen macroscopically. Bastites can be also identified based on their low content of Fe oxides. Indeed, in hand specimen, the zones without magnetite or hematite usually correspond to areas of bastite texture (Fig. 4c). We also note that bastites exhibit a straight extinction aligned with the cleavages.

In the mesh zones, Fe content decreases from the core to the edges (Fig. 4e, f). This Fe zonation corresponds to a zonation in crystallinity, where the core is mainly chrysotile and the edge is lizardite as observed in Raman micro-spectroscopy (Fig. 4g, h) where chrysotile only shows one peak at 3695 cm^{-1} whereas lizardite shows two peaks at 3684 cm^{-1} and 3704 cm^{-1} (Schwartz *et al.*, 2013). Unlike lizardite, chrysotile is commonly associated with magnetite. We note that only one crystal of antigorite was found in a vein. Zonation in Fe oxides can be observed in A1*, from the edge of the clast (hereafter, referred to as zone 1 of A1*) toward the center, where Fe oxides are rare. In the lower part of the thin section, Fe oxides are more abundant (hereafter, referred to as zone 2 of A1*), leading to the dark green color of the thin section (Fig. 4a). Different mesh zones are separated by serpentine veins with euhedral Fe oxides. We note that 100−500 μm sparitic calcite grains (hereafter, referred to as

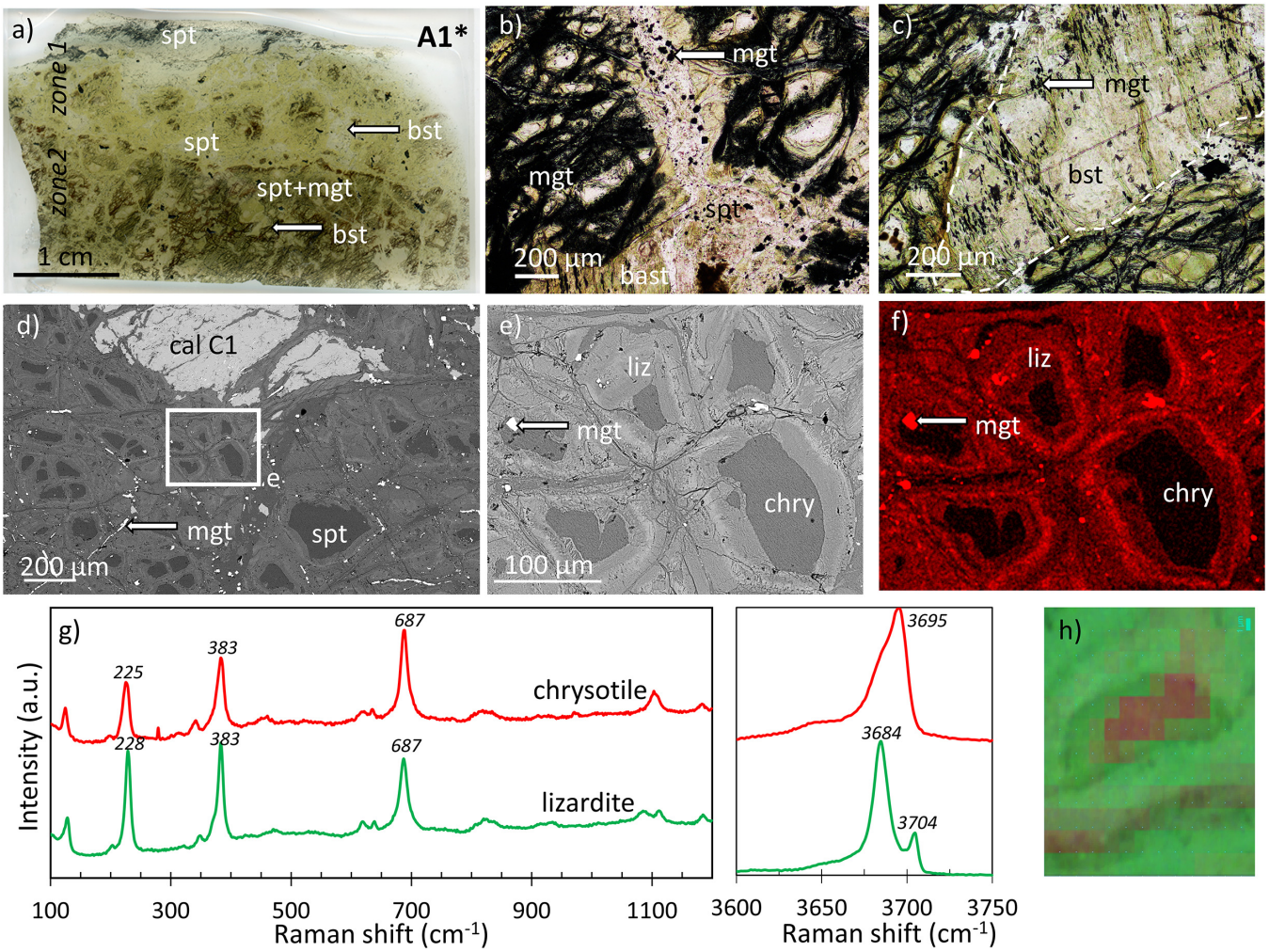

Fig. 4. (a) Thin section of sample A1*. (b) PPL (Plane Polarized Light) image of a serpentine vein with magnetite grains. (c) Magnified view of a bastite. (d) SEM image of the mesh texture. (e) Magnified image of the mesh texture and (f) associated Fe kα map. (g) Raman spectra of chrysotile and lizardite and (h) Raman map of chrysotile (in red) and lizardite (in green) in mesh. bst: bastite; cal: calcite; chry: chrysotile; liz: lizardite; mgt: magnetite; spt: serpentine.

C1; see Tab. 1 for nomenclature) are present in zone 1 of A1* (Fig. 4d).

The zonation in Fe oxides is also evident in red clasts (Fig. 2b). Three zones have been identified in sample B2* (Fig. 5). In zone 1, few Fe oxides are present and they are located at the edge of the mesh or crosscutting the mesh. As for A1*, the characteristic mesh texture can be observed. Some mesh zones next to the calcite veins, however, contain Fe-rich cores due to the veins of serpentine that crosscut the mesh (Fig. 5c). Some of these veins are spatially related to the massive serpentine vein occurring as a clast (hereafter, referred to as S1') in the calcite vein that is several millimeters thick (hereafter, referred to as C1') and in the border between the mesh and C1'. We note that the presence of bastites is highlighted by their higher Cr content than in the serpentine mesh (Fig. 5b). Bastites are ~100 µm in size and sometimes associated with calcite.

The second zone in sample B2* corresponds to the reddish zone, enriched in micrometric hematite with texture similar to zone 1. Hematite mainly occurs in the mesh but can also be observed in some cores associated with chrysotile. It is not clear whether magnetite is replaced by hematite. The third zone in sample B2* is more pristine with fewer Fe oxides. Some mesh cores are poorly crystallized and correspond to proto-serpentine. We also observed some voids in the cores. It is not clear whether these voids are an artefact of the polishing of the proto-serpentine or if there really are voids in some cores within zone 3. Voids were observed in different preparations of the same zone, in both thin and thick sections, favoring the interpretation that they are a true feature and not a result of sample preparation.

At the macroscopic scale, serpentine is associated with calcite in veins that crosscut clasts of type I ophicalcites (Fig. 6a, d). The transition from serpentine to calcite can be observed in sample B1*, where serpentinite is crosscut by a vein of massive serpentine (hereafter, referred to as S1) with replacive calcite (hereafter, referred to as C2). The grains of calcite are anhedral and vary in size from 200 to 500 µm. In addition, a 50-µm-wide vein (hereafter, referred to as C5') can be observed at the boundary between the main vein and the serpentinite. In cathodoluminescence (Fig. 6e), we were able to

Table 1. Nomenclature of all calcite and serpentine phases.

Name	Textural characteristics	Sample
$C1_{all}$		
C1	Sparitic calcite pervasively replacing some serpentine	A1*
C1'	Massive vein of calcite with sparitic grains of calcite	B1*
C1"	Calcite present in the matrix replacing some serpentine	D1*
$C2_{all}$		
C2	Sparitic calcite grains replacing serpentine	B2*
C2'	Calcite in the matrix of the breccia	E1*
C3	Sparitic calcite next to or in the vein of massive serpentine ($C3_{sparite}$)	D1*
C4	Dendritic calcite surrounding sparitic calcite C3	D1*
$C5_{all}$		
C5	Massive vein of calcite with sparitic grains of calcite associated to hematite	C1*
C5'	Veinlet of calcite which crosscuts all of sample E3* associated with hematite	B1–2*
S0	Mesh of serpentine and bastites	All samples
$S1_{all}$		
S1	Massive serpentine pervasively replaced by calcite	B1*
S1'	Clasts of massive serpentine in a vein of calcite	B2*
S2	Massive serpentine with dominant chrysotile which crosscuts all phases except C3	D1*

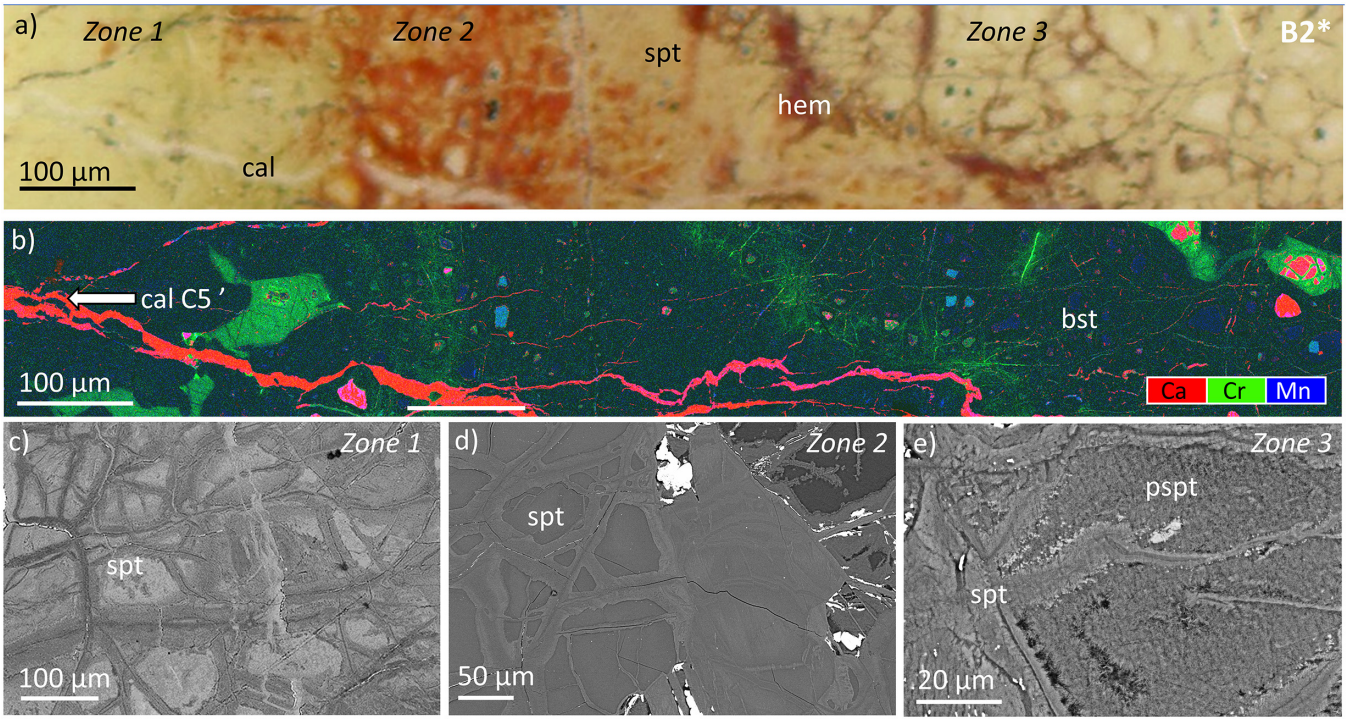

Fig. 5. (a) PPL image of B2* serpentinite clast (zone of interest delimited in Fig. 3c) and (b) the associated composite X-ray map of Ca Kα (red), Cr Kα (green), Mn Kα (blue). (c–e) SEM images of the serpentine mesh from the outer to the inner zones of the clast. cal: calcite; hem: hematite; pspt: proto-serpentine; spt: serpentine.

distinguish the different calcites based on their color: C5' exhibits an intense orange color, whereas C2 is darker. We also note that the grain boundaries of C2 are brighter than the cores. This difference in color is related to the chemical composition of the calcites. We suggest that the presence of Fe inhibits cathodoluminescence, whereas the presence of Pb or Mn favors it. We did not fully investigate the reason for this difference between the calcites and used it only as a diagnostic tool. In some locations, the vein C5' crosscuts the carbonated vein C1' and the clasts of serpentinite (Fig. 6f). Hematite was also found in association with C5'.

In the more hematite-rich samples (*e.g.*, C1*), where all serpentinite clasts are red at the sample scale, some reddish veins are present (Fig. 6c). This color is due to the presence of

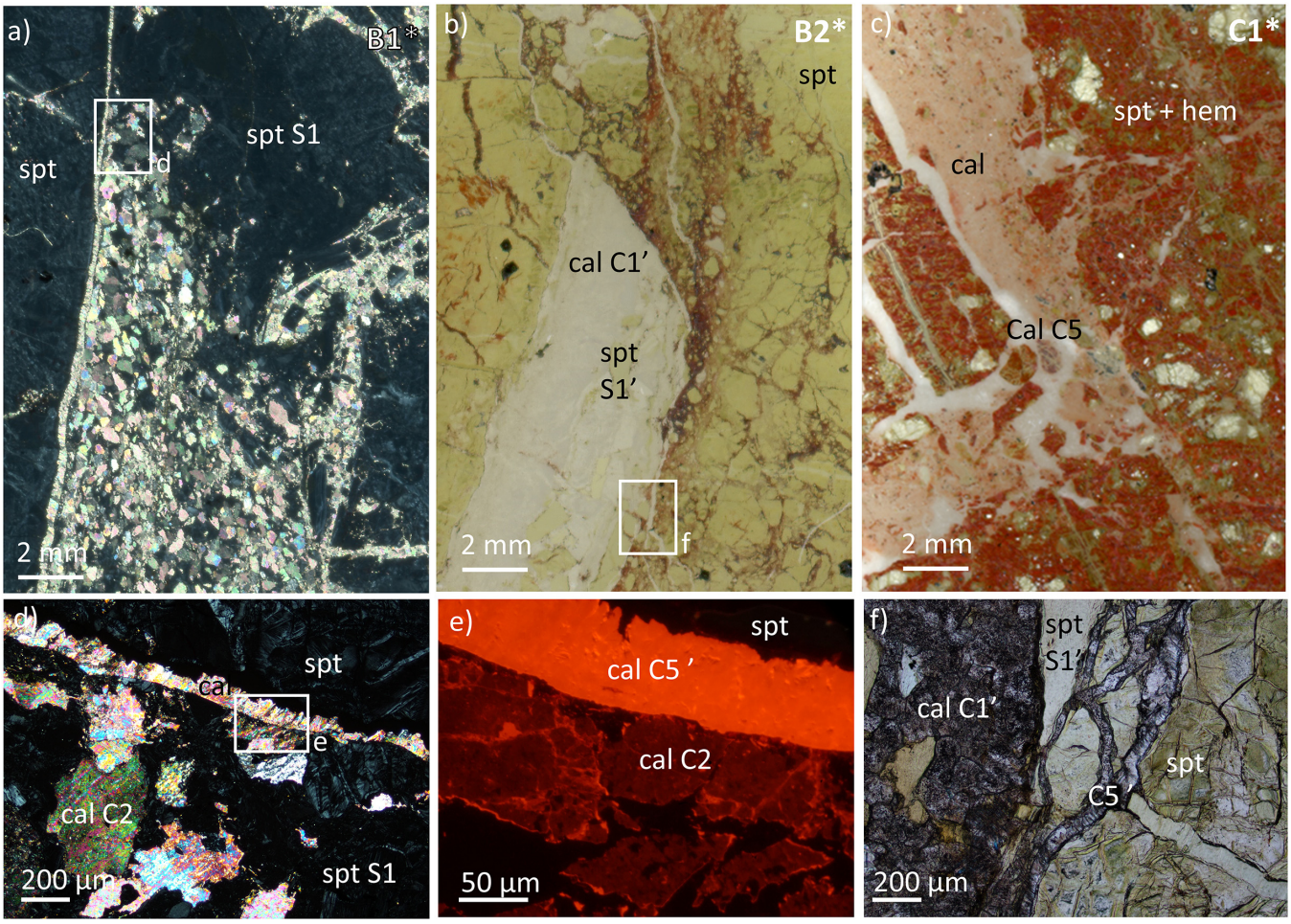

Fig. 6. (a) XPL (Cross Polarized Light) image of partially carbonated serpentine vein from B1*. (b) PPL image of carbonated serpentine vein crosscut by veinlet of calcite and hematite from B2*. (c) PPL image of reddish vein of calcite and hematite bordered with vein of calcite from C1*. (d) Magnified view (with 90° rotation) of (a) with (e) a zoom in the zone represented by the white square in cathodoluminescence (d). (f) PPL image of the border between the calcite vein and serpentine mesh crosscut by a calcite veinlet. cal: calcite; spt: serpentine.

some micrometric grains of hematite in association with calcite. This reddish vein is crosscut by a white vein corresponding to calcite with crystals ~200 µm in width.

In addition to Fe oxides associated with serpentine, we observed some chromites with a border of magnetite microcrystals. Some 100-µm-sized grains were also found to be completely replaced by magnetite at their borders (Fig. 7a). Trace amounts of several sulfides are present associated with calcite in sample B2*, with sizes ranging between 20 and 50 µm; these include Fe-vaesite ($(Fe,Ni)S_2$) associated with pentlandite ($(Fe,Ni)_9S_8$), chalcopyrite ($FeCuS_2$), and native sulfur associated with an undetermined late Fe-rich silicate. This latter phase could be ilvaite ($CaFe_3Si_2O_8(OH)$) associated at the microscale with some sulfides, but more analyses are needed to well determine its composition. The sulfides are anhedral and display corrosion textures. Bravoite ($(Fe,Ni,Co)S_2$) surrounded by Ni(Fe,Co) silicate was also observed in serpentine. Additionally, pyrite crystals were found in some of the voids and exhibited a framboidal-like texture.

4.1.2 Type II ophicalcite

Type II ophicalcites include carbonated clasts of serpentinite (smaller than those in type I ophicalcites) within a matrix of calcite and serpentine. A partially carbonated clast from a type II ophicalcite (sample D1*) is presented in Figure 8b. The pristine shape of this clast is evidenced by the boundary between the fine-grained matrix and the coarse-grained replacement calcite within the clast. This distinction between grain sizes can be seen in Figure 8a, where whiter zones correspond to replaced clasts. We can therefore use these observations to define an approximate boundary between calcite and serpentine.

This ophicalcite (sample D1*) is crosscut by a vein of massive serpentine (hereafter, referred to as S2). It corresponds to chrysotile with a low lizardite content. S2 contains coarse grains of calcite (hereafter, referred to as C3), which are euhedral in shape and nearly 1 mm in size (Fig. 8c). In cathodoluminescence (Fig. 8d), the color of these grains is orange with a brighter edge. When the vein crosscuts

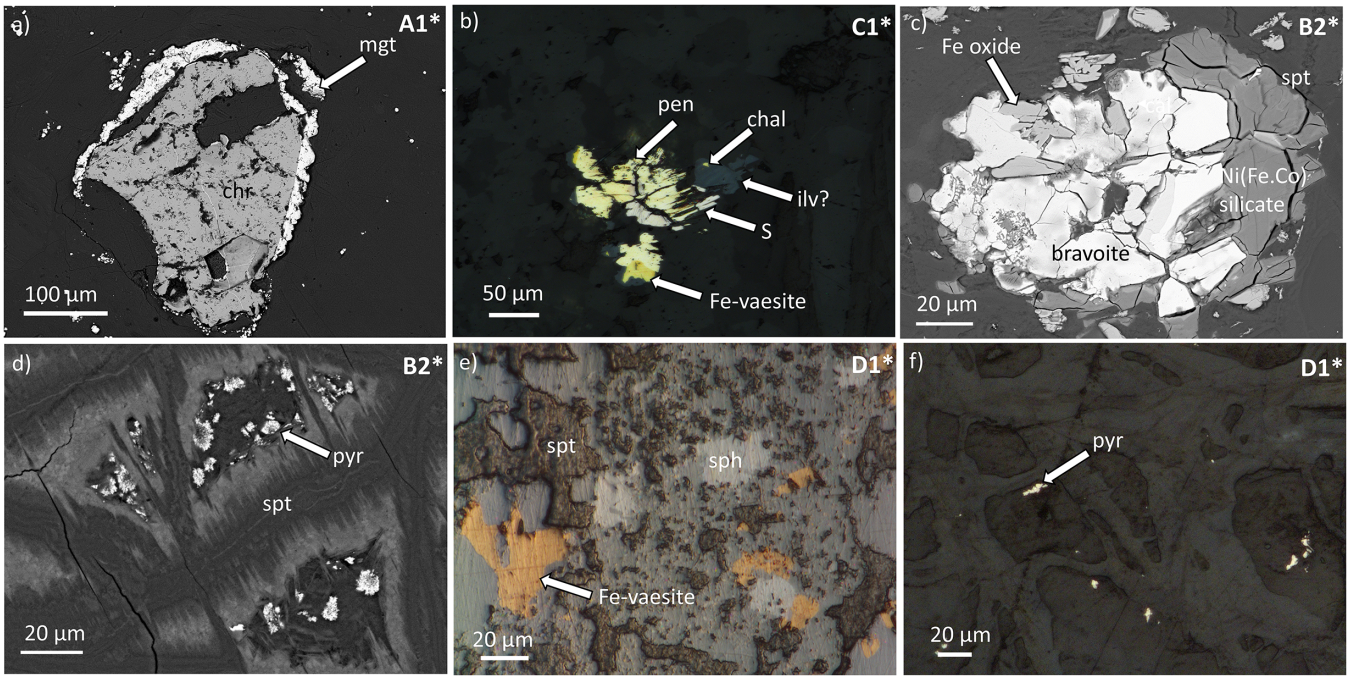

Fig. 7. (a) A chromite grain bordered with magnetite from A1*. (b) Image in reflection of opaque minerals in B2*. (c) SEM image of a bravoite grain bordered by Ni(Fe,Co) silicate and Fe oxide in B2*. (d) SEM image of pyrite present in cores of the mesh of serpentine in B2*. (e) Image in reflection of Fe-vaesite and sphalerite and (f) some pyrite present in the cores of the mesh of serpentinite clasts in D1*. cal: calcite; chal: chalcopyrite; chr: chromite; ilv: ilvaite; mgt: magnetite; pen: pentlandite; pyr: pyrite; sph: sphalerite; spt: serpentine.

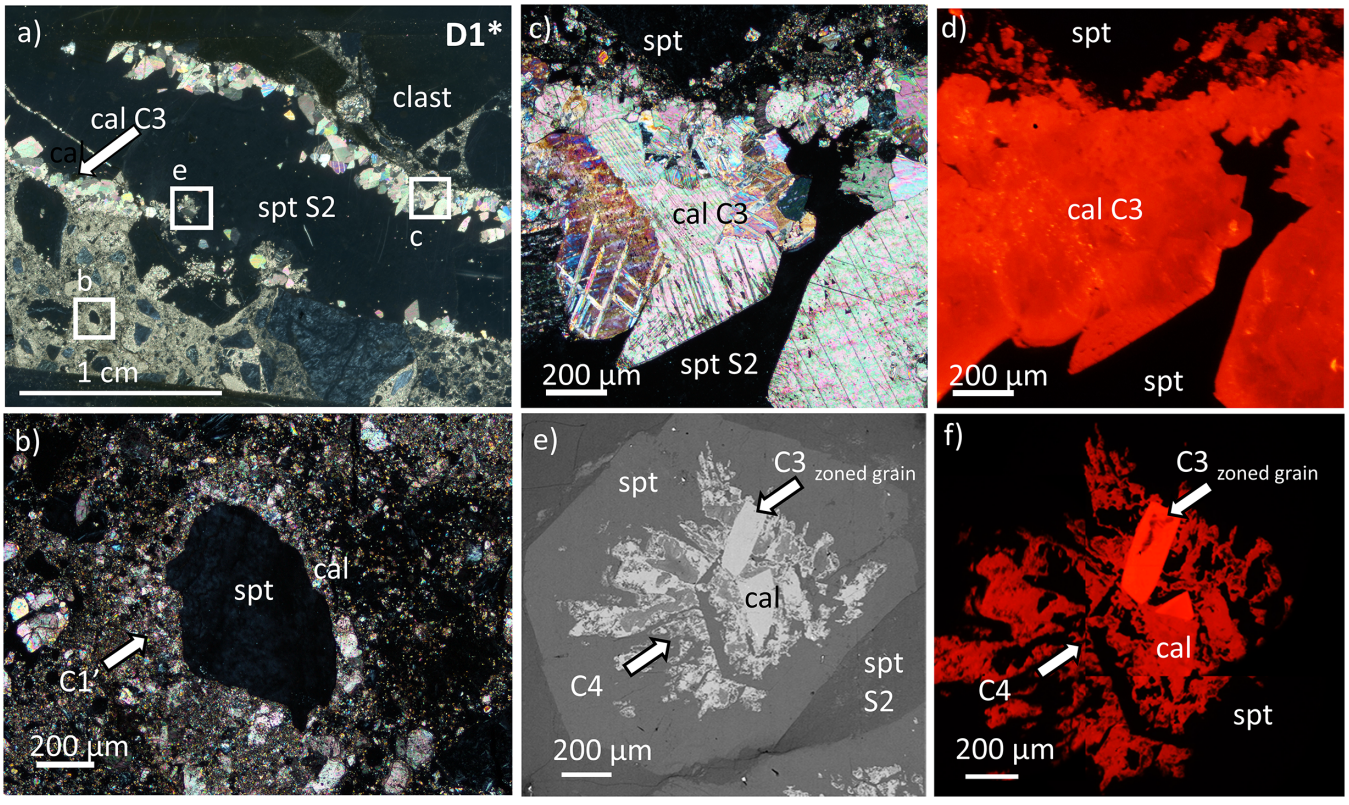

Fig. 8. (a) XPL image of D1* and (b) magnified view of the partially carbonated clast; (c) euhedral grains of calcite at the border of the S2 serpentine with (d) the associated cathodoluminescence image; (e) a grain of serpentine with euhedral and dendritic calcite at the border of the S2 serpentine with (f) the associated cathodoluminescence image. cal: calcite; spt: serpentine.

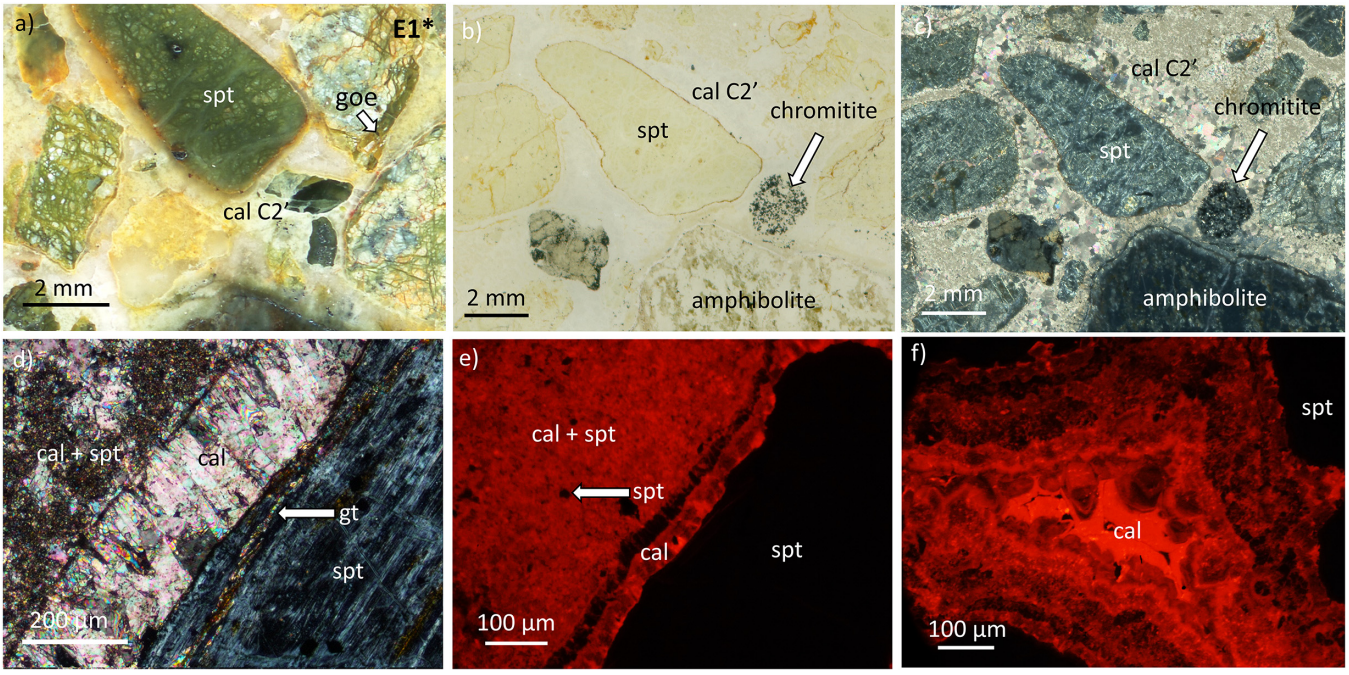

Fig. 9. (a) E1* sample with a brownish matrix revealing the presence of goethite and (b, c) PPL and XPL of the polygenic breccia with different clasts (serpentinite, chromitite, amphibolite). Micritic and sparitic calcite can be distinguished in the XPL image. (d) XPL image of the carbonated border of a clast and the micritic calcite and residual serpentine in the matrix. (e, f) Images acquired in cathodoluminescence of a carbonated border of a serpentinite clast and authigenic calcite in the matrix. cal: calcite; goe: goethite; spt: serpentine.

serpentinite clasts, calcite is less abundant and occurs inside the euhedral serpentine (Fig. 8e). Two types of calcite can be distinguished: (1) euhedral calcite similar to the coarse grains present in the vein of serpentine S2, and (2) dendritic calcite associated with serpentine. In cathodoluminescence, the dendritic calcite is duller than the coarse grains toward the center (Fig. 8f). We commonly observed euhedral Fe-rich serpentine between two generations of dendritic calcite. Sphalerite (ZnS) and Fe-vaesite are locally associated with calcite in the matrix (Fig. 7e). Similar to observations in type I ophicalcites, some chromites are variably replaced by magnetite. Pyrite is also present in the mesh of some clasts, typically in the form of elongated crystals (20 µm).

4.1.3 Type III ophicalcite

Type III ophicalcites correspond to a polygenic breccia with clasts of serpentinite, amphibolite, and chromitite (Fig. 9b, c), embedded in a matrix of fine-grained calcite (hereafter, referred to as C2') with some micrometric serpentine (Fig. 9d). The edges of the clasts in contact with the matrix are commonly bordered by sparitic calcite (100–200 µm). Maximum calcite widths are found closest to the clasts. In cathodoluminescence, an outer dark border and an inner bright vein can be seen. Zonation can be occasionally observed in cathodoluminescence, typical of authigenic calcite (Fig. 9f). In addition, some orange Fe oxides, corresponding to goethite (FeO(OH)), crosscut both the matrix and clasts. The outer part of the clasts is orange in color; this can also be observed macroscopically (Fig. 9a).

4.2 Geochemistry

4.2.1 Element geochemistry

4.2.1.1 Serpentine

4.2.1.1.1 Major elements

Bastites are characterized by their high Al_2O_3 (0.40–1.74 wt %) and Cr_2O_3 (0.17–0.88 wt%) contents. By mapping the bastites, we were able to observe the shape of the altered primary pyroxenes with a size of approximately 100 µm (Fig. 5b).

Varied contents of $FeO + Fe_2O_3$ (hereafter, FeO*) were measured within the mesh cores (mainly corresponding to chrysotile) across the samples, in the range 1.04–6.70 wt%. In sample A1*, FeO* content differs between zone 1 and zone 2, where zone 2 has a higher magnetite content. The zone 1 mesh cores have a FeO* content of 1.04–4.40 wt%, compared with 3.72–5.63 wt% in zone 2 mesh cores. A measured point in a magnetite-rich zone within the mesh core of zone 1 was found to have a FeO* content of 5.70 wt%. In this sample, the mesh cores are mainly enriched in MgO; however, we also observed MgO-depleted mesh cores, particularly in hematite-rich samples. Bastites contain FeO* in the range 4.11–6.16 wt%, similar to the lizardite of serpentine mesh. The vein S1 has a similar FeO* content to the B2* mesh cores, consistent with the observation that some serpentine veins have the same grey color as the mesh cores (Fig. 5c). The S2 vein has a FeO* content of 3.42–3.80 wt%.

4.2.1.1.2 Minor elements (Ni, Cl, F)

Ni, Cl, and F are some of the elements that may replace others in serpentine. Ni is more frequent in lizardite,

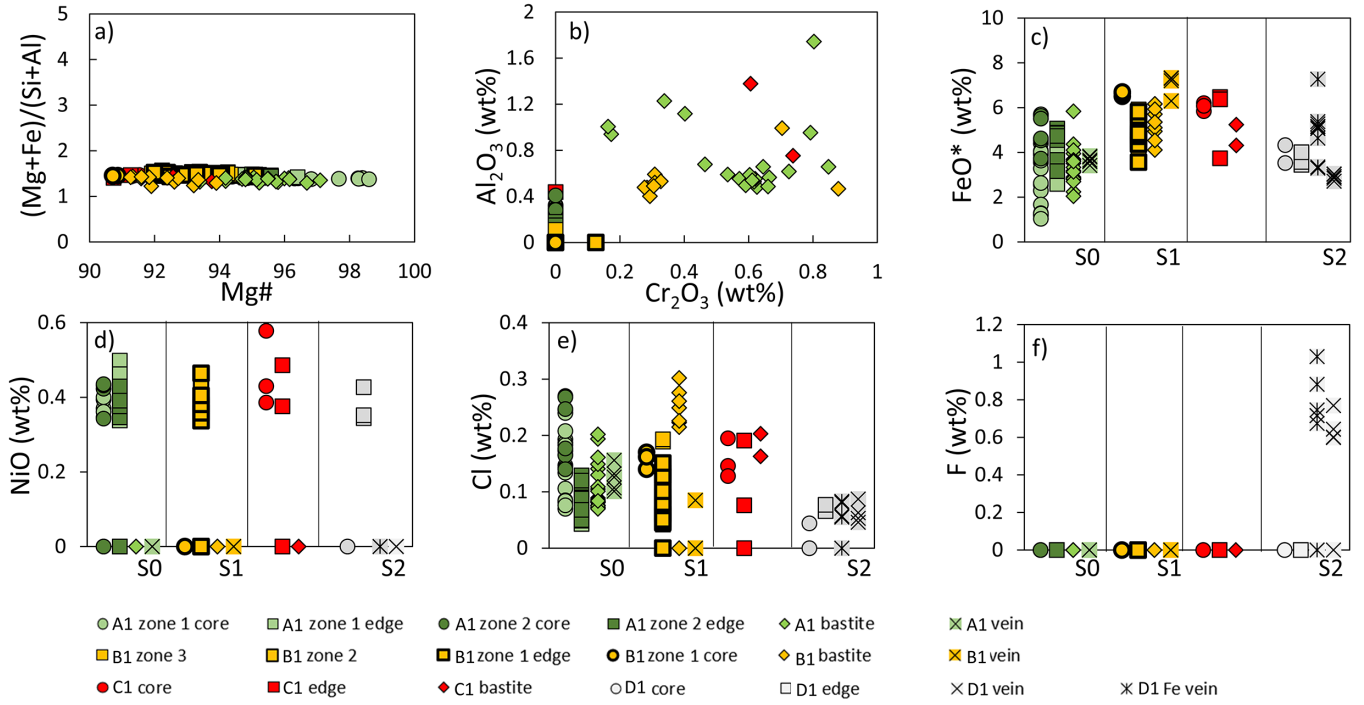

Fig. 10. Chemical compositions of the serpentines. (a) (Mg + Fe)/(Si + Al) ratio *versus* Mg/(Mg + Fe) noted as Mg#. (b) Al_2O_3 oxides *versus* Cr_2O_3. The bastites are enriched in those oxides compared to the serpentines replacing olivine. (c–f) Abundances of FeO*, NiO, Cl and F. When a value was below the detection limit of an element, it was set to 0, which explains the basal trends.

occasionally occurs in chrysotile of serpentine mesh, but was not observed in bastites or within the veins. When detected, NiO has a content of approximately 0.4 wt%. The Cl contents are higher in the mesh cores than at the edges. The Cl content in bastite is either similar to, or higher than, the Cl content within the mesh cores, as observed in the bastites from the B2* sample. F was only detected in the S2 vein in the range 0.60−0.77 wt%. The F content is higher (up to 1.02 wt%) in the Fe-rich serpentine located in vein S2. It is not clear whether this is an accurate F content for the sample or is related to contamination during sample preparation. However, the fact that the total oxide content is around 85 wt% minimizes the impact of pollution on the F measurement (Fig. 10).

4.2.1.2 Calcite

4.2.1.2.1 Major elements

The chemistry of different recorded carbonate phases likely corresponds to nearly pure calcite, with average and maximum MgO contents of 0.43 wt% and 1.24 wt%, respectively. This maximum is not correlated with an increase in SiO_2 content. Some analyses show an increase in Al_2O_3 up to 1.74 wt%, correlated with an increase in MgO up to 1.98 wt %, which we suggest may be related to the presence of spinel. Notably, FeO was not detected in calcite.

4.2.1.2.2 Minor elements (Mn, Na, F)

MnO was detected in calcites from the sample D1* in the range 0.38−0.48 wt%. Na_2O and F were also detected in some calcites of sample D1*. Similar to the measurements of F in serpentine, it is not clear whether the presence of these minor elements can be attributed to contamination during sample preparation.

4.2.1.3 Fe speciation

The ^{57}Fe Mössbauer spectra exhibit various signals (sub-spectra) associated with iron oxides (magnetite ($Fe^{2+}Fe^{3+}{}_2O_4$), hematite ($Fe^{3+}{}_2O_3$), maghemite (γ-$Fe^{3+}{}_2O_3$), chromite ($Fe^{2+}Cr_2O_4$)), iron oxyhydroxide (goethite ($Fe^{3+}O(OH)$)), and Fe-rich phases (serpentine ($(Mg,Fe^{2+},Fe^{3+})_3(Si,Fe^{3+})_2O_5(OH)_4$)) (Fig. S1). The relative proportions of each component (Fe^{2+} or Fe^{3+}) extracted from the fitting of experimental data are presented in Table 2. Serpentine is the main mineral containing Fe in each sample. In the main veins, where the powder represents only one phase, the Fe^{3+}/Fe_{tot} ratio of serpentine is 0.31 for S1' and for S2. Hematite contents of several percent are associated with S1', whereas magnetite is associated with S2. In multi-mineral assemblages, the Fe^{3+}/Fe_{tot} ratio ranges between 0.49 and 0.68. Type II ophicalcite (D1*) contains only magnetite, whereas both magnetite and maghemite were found in type I ophicalcite (A1*). C1* and B2* contain only hematite as Fe oxide. Type III ophicalcite (E1*) contains maghemite and goethite. Furthermore, a positive correlation was observed between the Fe^{3+}/Fe_{tot} ratio of serpentine and the bulk Fe^{3+}/Fe_{tot} ratio (Fig. 11).

4.2.2 Isotope geochemistry

4.2.2.1 Stable isotopes (C, O)

Carbon and oxygen isotopes were measured in the main calcite veins (Fig. 12). Two main endmembers were detected: (i) $\delta^{18}O \sim 18‰$ and $\delta^{13}C \sim -2‰$, and (ii) $\delta^{18}O \sim 30‰$ and $\delta^{13}C \sim -2‰$. A third pole was also defined, with $\delta^{18}O \sim 23‰$ and $\delta^{13}C \sim -18‰$; this corresponds to a single zoned calcite grain present in the vein C1'.

Table 2. Relative proportions (%) of each Mössbauer sub-spectrum extracted from analysis of the experimental data collected at room temperature, and Fe^{3+}/Fe_{tot} ratios (%) of the serpentine and the bulk powder.

	A1*	B2* zone 1	B2* zone 3	B2* (S1')	C1*	D1*	D1* (S2)	E1*
Serpentine Fe^{2+}	18	16	41	63	22	37	64	25
Serpentine Fe^{3+}	30	35	41	28	30	36	29	39
Chromite Fe^{2+}	4	0	5	5	0	6	6	3
Hematite	0	49	13	4	48	0	0	0
Magnetite	28	0	0	0	0	20	0	0
Maghemite	21	0	0	0	0	0	0	23
Goethite	0	0	0	0	0	0	0	9
Fe^{3+}/Fe_{tot} serpentine	**62.7**	**50.4**	**68.2**	**30.9**	**58.0**	**49.3**	**31.3**	**61.1**
Error (2σ)	14.2	8.0	14.0	5.8	12.4	8.2	5.3	11.0
Fe^{3+}/Fe_{tot} bulk	**69.2**	**54.3**	**83.7**	**32.3**	**78.0**	**49.7**	**29.3**	**79.0**
Error (2σ)	18.5	13.2	13.6	10.1	13.0	11.0	5.7	22.0

The lowest $\delta^{18}O$ values (Tab. 3) are present in the vein C5' associated with hematite, and in the vein C5 crosscutting the hematite-rich samples. Low $\delta^{18}O$ values are also present both in the matrix of the type II ophicalcite (D1*) and the dendritic calcite (Fig. 8e). Notably, the highest $\delta^{18}O$ values (~30‰) are associated with calcites C2 (sample B1*), C2' (sample E1*), and C3 (sample D1*). Intermediate $\delta^{18}O$ values were observed in samples A1* and B2*. The $\delta^{13}C$ values are broadly consistent, ranging between −5‰ and 0‰. However, the $\delta^{13}C$ values from the type II ophicalcite are lower than in the other samples, for which $\delta^{18}O$ values are around 30‰.

4.2.2.2 Temperature of carbonation

In order to discuss the origin of different calcites (no dolomite was observed), it is crucial to define their carbonation temperatures using oxygen isotopes. To obtain these temperatures, we used the fractionation law determined by Kim and O'Neil (1997);

$$1000 \times \ln\left(\alpha_{calcite-water}^{^{18}O-^{16}O}\right) = 4.01 \times \frac{10^6}{T^2} - 4.66 \times \frac{10^3}{T} + 1.71. \quad (2)$$

To complete the equation, the unknown $\delta^{18}O$ of water must be defined. This requires an assumption of the carbonation time period. Previous work has shown that the Sivas ophiolite has a geological history similar to that of the Oman ophiolite, in terms of both its timing of formation and its obduction during the Late Cretaceous (Legeay *et al.*, 2019). Additionally, carbonation of the ophiolite is known to occur mainly at the seafloor (Schwarzenbach *et al.*, 2013). Thus, we can assume that $\delta^{18}O$ of water during carbonation had a value of 0‰, defined as the value of Cretaceous seawater (Pucéat *et al.*, 2003; Veizer and Prokoph, 2015).

After applying Equation (2), the carbonation phases in the studied samples likely occurred at temperatures ranging from 25 °C to 100 °C. This temperature range suggests that no isotopic resetting occurred, otherwise all temperature values would depend directly on the degree of metamorphism as interpreted by Bernoulli and Weissert (2021). Moreover, no zonation in $\delta^{18}O$ was observed in calcite grains. The calcites C2, C3, and C5 have specific carbonation temperatures around $36 + 6/-5$ °C, 34 ± 1 °C and $91 + 3/-2$ °C, respectively. The other values fall between these endmembers. The different events within the carbonation sequence will be discussed further in the following sections.

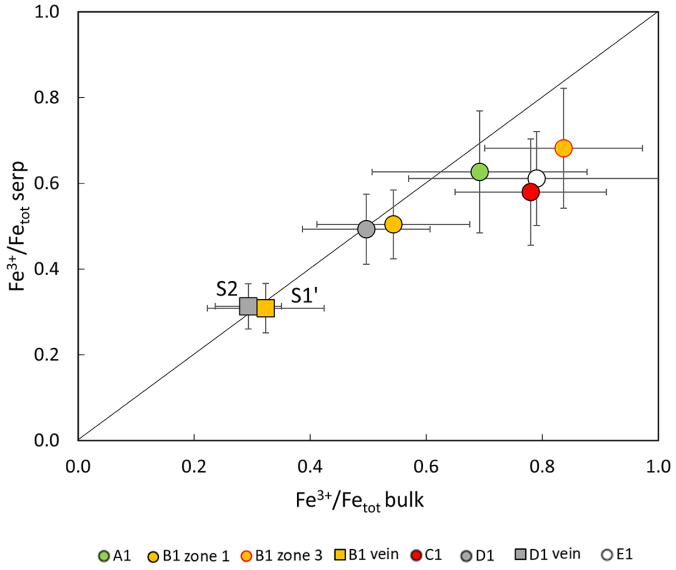

Fig. 11. Fe^{3+}/Fe_{tot} ratio of serpentine plotted *versus* bulk Fe^{3+}/Fe_{tot} ratio of sample.

5 Discussion

The contacts between different phases of calcite and serpentine allow us to construct a chronology of alteration. An initial serpentinization event occurred before repeated carbonation events, followed by a late serpentinization event. We first discuss this early serpentinization episode, followed by

Table 3. C and O isotopic data for calcites and estimated temperature of precipitation. Error is given in 2σ.

Calcite name	$\delta^{13}C$	$\delta^{18}O$	T (°C)
C1	-2 ± 0.7	23.5 ± 1.8	62 +11/-10
C1'	-2.9 ± 1.3	24.4 ± 1.1	57 ± 6
C1' $_{\text{zoned grain}}$	-10.9 ± 1.8	24.0 ± 0.7	59 ± 4
C1"	-2.5 ± 0.7	22.7 ± 1.8	66 +12/-10
C2	0.2 ± 0.9	28.7 ± 1.2	36 +6/-5
C2'	-0.2 ± 0.7	29.5 ± 0.5	32 ± 2
C3	-3.2 ± 0.5	29.2 ± 0.3	34 ± 1
$C3_{\text{zoned grain}}$	-2.9 ± 0.8	26.9 ± 2.5	44 +13/-12
C4	-1.8 ± 0.5	18.6 ± 1.1	96 ± 9
C5	0.3 ± 0.5	19.2 ± 0.4	91 ± 3
C5'	-1.9 ± 1.5	19.0 ± 0.3	92 ± 2

constraining the conditions during the different carbonation events. Finally, we discuss the last serpentinization event and the geological context in which it occurred.

5.1 Early serpentinization

5.1.1 Protolith

Primary minerals are absent in the serpentinite clasts. This means that the altered peridotite samples were completely serpentinized prior to brecciation. Despite the absence of primary minerals, the bastite content allows us to determine the initial pyroxene content. The modal proportion of bastites is approximately 25%. We interpret the straight extinction with reference to their cleavages as a relic of the typical extinction of orthopyroxene. We did not observe any bastites with an oblique extinction. Therefore, we propose that the protolith of the ophicalcites is harzburgite, consistent with literature (Parlak, 2016; Kavak *et al.*, 2017).

5.1.2 Evolution of serpentinization

Serpentinization is both spatially and temporally variable (Oufi *et al.*, 2002; Bach *et al.*, 2004; Rouméjon and Cannat, 2014; Noël, 2019). Generally, the mantle peridotites are first altered by seawater during their exhumation, passing from high-temperature zones (>350 °C) near the MOR to cooler zones. This exhumation process leads to 70−75% serpentinization (Oufi *et al.*, 2002). Commonly, the first phase of serpentinization involves formation of a mesh, where lizardite replaces the edges of fractured olivines and pyroxenes. During the second phase, chrysotile replaces the remaining cores of olivines and magnetite commonly evolves. This serpentinization sequence has been previously described in the literature (Bach *et al.*, 2006) and was typically observed in serpentinite clasts of type I ophicalcites of the Sivas ophiolite. Lizardite is present in bastites and at the edges of the mesh, whereas chrysotile is observed in the cores as well as in veins in association with magnetite.

There is only one occurrence of antigorite, and this is located within a vein. Its presence could be the result of local Si-metasomatism due to the serpentinization of pyroxene at depth (O'Hanley, 1992; Rouméjon *et al.*, 2015; Schwartz *et al.*, 2013). We did not investigate further the origin of the antigorite owing to its scarcity. We suggest, however, that the presence of antigorite could be consistent with the presence of some bastites in the veins, perhaps indicating previous formation of pyroxenite veins that localized fluid flow. NiO is only present in serpentine (not in bastite) and approximately constant in volume when present, at ∼0.4 wt%. The low NiO content could be explained by pervasive replacement of former olivine and/or by the multiplicity of recrystallization events (Rouméjon and Cannat, 2014). This is consistent with the absence of talc, tremolite, or brucite, which can be explained by continued fluid–rock interactions resulting in changes in fluid pH and silica activity, and reaction of these phases to serpentine (Bach *et al.*, 2004). Hence, the absence of these minerals suggests an advanced stage of alteration, whereby only serpentine and Fe oxides remain. The lack of brucite can be explained in two ways: (i) a high Si content of the fluid, or (ii) a dissolution of brucite by late fluid–rock interactions (Bach *et al.*, 2006; Frost and Beard, 2007). However, The hypothesis (i) can be discarded because this would help stabilize talc and tremolite (Allen and Seyfried, 2003), phases that were not observed.

As observed by Noël (2019), we determined a domain where there is less magnetite, leading to some zonation in Fe oxides (sample B2*). Because the zonation is crosscut by the S1 vein, we suggest that this zonation results from an early serpentinization and traces the fluid flow path. In the zones with fewer or no Fe oxides, chrysotile cores can be replaced by late chrysotile with a higher Fe content. This Fe-rich serpentinization episode occurs mainly next to the S1 vein which has a similar Fe content, so we propose that these episodes are linked. This episode is similar to that described by Noël (2019).

5.1.3 Brecciation event(s)

It is common to observe carbonate-filled fractures in ophicalcites related to a brecciation event (Artemyev and Zaykov, 2010; Lafay *et al.*, 2017; Schwarzenbach *et al.*, 2013). It is rare, however, to observe massive serpentines like those seen in sample B1* filling the fractures. According to the clast morphology, the clast size, and the presence of veins filled with crystallized serpentine, a large-scale brecciation associated with S1 could have been produced by either

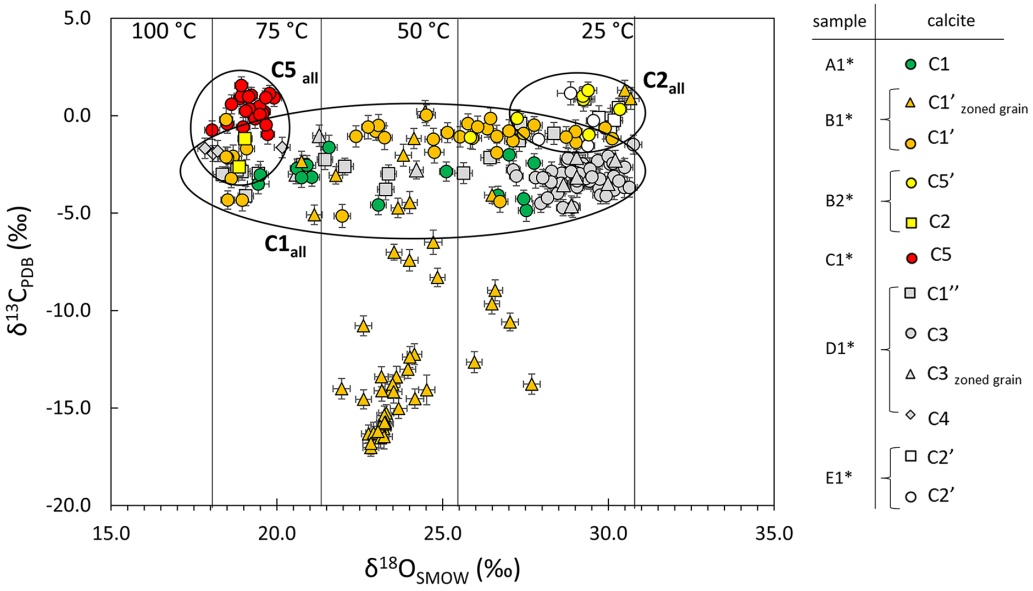

Fig. 12. $\delta^{18}O$ against $\delta^{13}C$ compositions of calcites from the Sivas ophiolite. The estimated temperatures of precipitation of calcite are also presented for discussion.

(i) hydro-fracturing or (ii) small-scale reaction-induced fracturing processes (Renard, 2021; Taber, 1916; Wiltschko and Morse, 2001). The systematic presence of massive serpentine S1 in type I ophicalcite (Figs. 2c and 3b) reflects the first crystallization phase within the voids created by fractures before calcite replacement. This is in favor of model (ii), where the crystallization of serpentine would have led to fracturing, but we cannot eliminate model (i). The geological context for this brecciation is unclear. A detachment fault is usually proposed to explain the origin of brecciation (Cannat *et al.*, 2010; Rouméjon and Cannat, 2014). As the ophicalcite evolved from type I to type II over several dozens of meters, it is difficult to infer a detachment fault as a source; instead, we propose that this brecciation likely occurred in the fault damage zone. We did not perform isotopic measurements on this serpentine to constrain its formation temperature, but we suggest that it formed at relatively low temperatures (150–200 °C) owing to its high Fe content and the absence of associated magnetite (Klein *et al.*, 2014).

It is likely that the brecciation occurred at the same time than type II ophicalcite formation (sample D1*). More intense brecciation can be associated with the zone closer to the fault damage zone. However, the ophicalcites studied here seem to have been formed by a tectono-sedimentary brecciation without massive crystallization in fractures. The origin of the residual serpentine in the matrix is unclear. It could have either crystallized within voids created by fractures such as S1, or resulted from finely brecciated serpentinite clasts. Sulfides that occur between the clasts in type I and type II ophicalcites are interpreted as the result of desulfurization of primary sulfides and a later precipitation during fluid-dominated serpentinization (Paulick *et al.*, 2006).

5.2 Carbonation events

Carbonation of the studied samples is heterogeneous, where samples near the top of the ophiolitic succession (Fig. 2) are more carbonated (*i.e.*, samples C1* and E1*). This supports that this upper part can be a major tectonic contact that channelized the hydrothermal fluid or a paleo-seafloor. The ophicalcites show a spectrum of carbonation intensity, from pervasive carbonation to the formation of calcite veins, as observed in literature (Picazo *et al.*, 2020; Schwarzenbach *et al.*, 2013).

5.2.1 Multiple carbonation events: cooling to reheating

Previous work suggested that serpentinization and carbonation of ophiolites, especially peridotites, occurs at the seafloor during and/or after exhumation (Andreani *et al.*, 2014; Noël, 2019; Lafay *et al.*, 2017). Here, we use petrological and isotopic data to constrain the timing of the low-temperature and high-temperature calcites, in order to construct a cooling and/or heating history for the serpentinized peridotites. We do not discuss here the Ca source because of the lack of relevant data. We can assume, however, that the Ca might derive from the breakdown of clinopyroxene during the hydration of peridotite and/or seawater.

5.2.2 Cooling

Other studies (*e.g.*, Lafay *et al.*, 2017) have shown that some ophicalcites record a continuum between serpentinization and carbonation, the latter beginning at temperatures of ~150 °C. We did not observe a continuum in our samples (Tab. 3), which favors separate carbonation and serpentinization processes (Coltat *et al.*, 2019, 2020). Moreover, after textural relationships, carbonates formation postdates serpentinization. We can then assume that after the first event of serpentinization leading to $S1_{all}$, a cooler fluid led to the formation of C1' at temperatures of 35−100 °C. The first carbonation event could have occurred during the exhumation of serpentinized peridotites to the seafloor. Indeed, one grain found in the C1' vein shows $\delta^{13}C$ values as low as ~−17‰. Such low $\delta^{13}C$

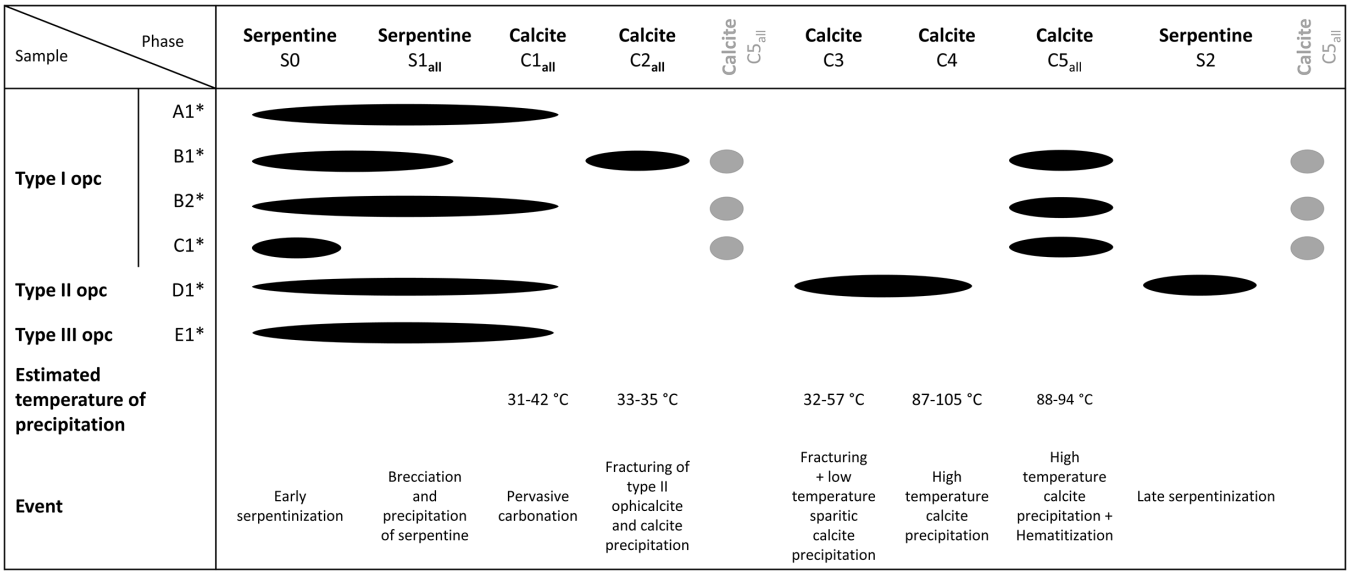

Fig. 13. Relative chronology of the different episodes of alteration. In grey color, are the possible scenarios for calcite $C5_{all}$.

can be explained by (i) local input of organically derived C decreasing the C isotopic value (White, 2015), or (ii) by Fischer–Tropsch reactions in serpentinization-derived fluids (McCollom and Seewald, 2007; Schrenk *et al.*, 2013) occurring during peridotite exhumation. Based on the carbon and oxygen isotopic values, we propose that the C1' calcite present in the matrix between serpentinite clasts was formed during the same event as C1 and C1". This is consistent with petrologic evidence, where the ophicalcite containing the calcites C1" in the matrix is crosscut by the sparitic calcite C3, which formed at low temperatures (~35 °C). The calcites $C1_{all}$ seem therefore related to cooling after the S1 serpentinization even if a carbonation during a different hydrothermal event cannot be ruled out.

5.2.3 Seafloor alteration

The second carbonation event is recorded by calcites with slightly enriched $\delta^{13}C$ compared to $C1_{all}$, with low precipitation temperatures (~35 °C). For example, C2 has pervasively replaced S1 (Fig. 6a), whereas C2' represents calcite that precipitated directly after brecciation of the serpentinites, chromitites, and amphibolites. Based on the study of Legeay *et al.* (2019), the amphibolites are dated at ~90 Ma and complete obduction occurred at 65 Ma. We can therefore estimate that the formation of C2' occurred 90–65 Ma ago, at the seafloor even if a post-obduction carbonation can still be possible.

5.2.4 Heating

Finally, the last low-temperature calcite is represented by C3. We suggest that this calcite did not form at the same time as $C2_{all}$, because it is related to a heating event. The ophicalcite D1* was fractured and first filled by C3 at the borders. Calcite and serpentines formed the zoned grains; the cores of sparitic calcites register formation temperatures of 32–57 °C, whereas the outer dendritic calcites formed at 87–105 °C. Such heating could occur in oceanic environment near the oceanic ridge. However, the fact that C2 and C3 postdate the amphibolite brecciation suggests that the rocks are not in such an environment. Instead, we propose that fluids could have been heated at depth (~3 km) circulating in a foreland setting for example between 55 and 40 Ma (Legeay *et al.*, 2019). After this period, the Sivas Basin sediments underwent rapid cooling (Darin *et al.*, 2018), suggesting that the heating we observed happened before 40 Ma. Therefore, we suggest a late hot fluid during the early Eocene could have altered the ophiolite.

We also discuss here the formation of the dendritic texture of C4 at high temperature. Although we chose to describe the texture as dendritic, this description can be confusing. The texture is often related to a fast change in temperature, but it can also result from oversaturation. The texture we observed is similar to that described by Hopkinson *et al.* (2000), who interpreted it as a result of carbonate replacement of serpentine. Even if such replacement can be assumed, we also suggest that, locally, alternating events of serpentinization and high-temperature carbonation could result in this dendritic texture, related to disequilibrium during precipitation of calcite C4. Further observations of this texture could better determine its true origin.

The C5 calcites could also have been formed during the late hot carbonation event that produced the C4 calcites. The C5 calcites recorded a higher oxidizing environment associated with hematite. We did not, however, observe any contact between calcites C4 and C5. Therefore, this hot carbonation event could have occurred between the C2 and C3 carbonation events, between the C4 and S2 alteration events, or just after the late S2 serpentinization event (Fig. 13). In all cases, this is a recent alteration event.

If the C3, C4, and C5 carbonation events occurred during the Eocene, we can also discuss the use of the oxygen isotopic value for Cretaceous seawater in Equation (2) (Pucéat *et al.*, 2003; Veizer and Prokoph, 2015). Evaporite formation suggests that the water source during the Eocene was likely to be from an ocean, whatever the mechanism responsible for the brine concentration (*e.g.* Gaucher, 2020; Warren, 2016).

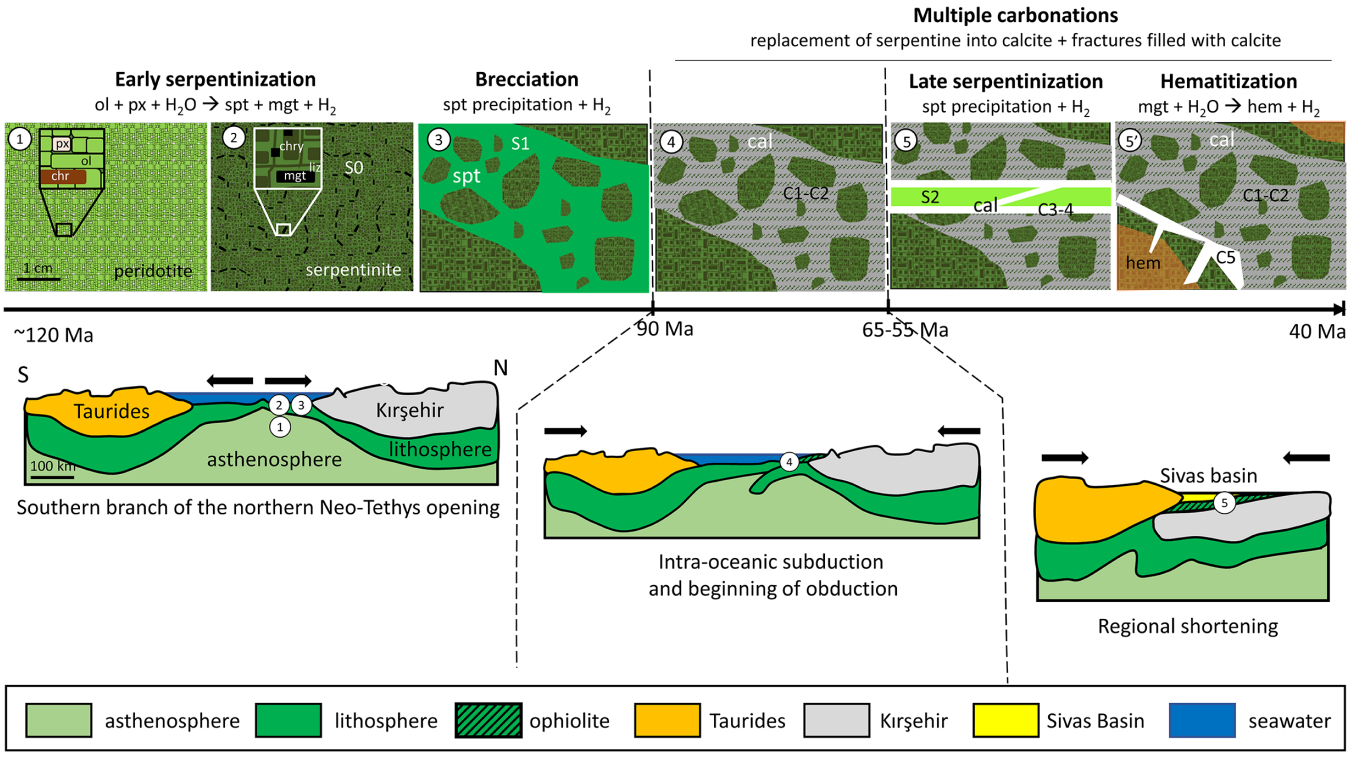

Fig. 14. Sketch of the different alteration events from the seafloor to the continent. cal: calcite; chr: chromite; chry: chrysotile; hem: hematite; liz: lizardite; mgt: magnetite; ol: olivine; px: pyroxene; spt: serpentine.

Based on Veizer and Prokoph (2015), the oxygen isotopic value of Eocene seawater is similar to the value of the Cretaceous seawater at about 0‰. Therefore, the estimated precipitation temperatures would not change.

Based on our observations, the chronology of the different episodes of serpentinization and carbonation events are summarized in Figure 13. This chronology highlights that serpentine S2 is the youngest phase.

5.3 Late serpentinization and H_2 potential

Only indirect evidence exists for continental serpentinization, particularly *via* hyperalkaline fluids resulting from the interaction of water and partially serpentinized ophiolites (Barnes *et al.*, 1967; Neal and Stanger, 1983; Abrajano *et al.*, 1988; Deville and Prinzhofer, 2016). Based on the normal geothermal gradient in the continent, around 30 °C/km, it is proposed that continental serpentinization happens at rather low temperatures, in the range 150–200 °C (Abrajano *et al.*, 1988; Etiope *et al.*, 2011; Moody, 1976; Neal and Stanger, 1983).

The S2 serpentine observed in Sivas ophiolites seems to result from a heating of fluids as described in the previous section, leading first to the formation of euhedral, dendritic calcite and serpentine. The S2 serpentine is massive, mainly corresponding to chrysotile, with a low Fe content and a low Fe^{3+}/Fe_{tot} ratio. The precipitation temperature of this serpentine remains unclear. The absence of magnetite still suggests that the temperature of serpentinization were below 200 °C, maybe between 150 °C and 200 °C which would be at the boundary with the high temperature carbonation associated to C4 calcite. We propose that this late serpentinization occurred after the obduction that led to the first carbonation events. Therefore, this serpentinization most likely took place in a continental environment. We suggest a likely tectonic environment for serpentinization would be the onset of shortening in the Sivas Basin, in a foreland setting between 55 and 40 Ma (Legeay *et al.*, 2019), as discussed in the previous section. The burying of ophiolites at several km deep would have favored the heating of fluids altering it.

Therefore, the formation of S2 occurred simultaneously with the deposition of Bartonian evaporites (Pichat, 2017; Pichat *et al.*, 2021). If confirmed by other analyses, this finding favors a possible causal relationship between serpentine and evaporite formation, through water pumping and dehydration of the foreland basin. Indeed, some models propose that serpentinization could lead to enrichment in fluid salinity, which could then precipitate as dehydratites (Debure *et al.*, 2019). Geochronology could be used to further constrain the timing of serpentine precipitation. Unfortunately, we found that the U and Pb contents were insufficient to allow dating of the calcites associated with the S2 serpentine phase and the associated heating.

5.4 Summary of the chronology

In summary, the harzburgite underwent both serpentinization and carbonation events. First, peridotites underwent a typical serpentinization S0 during exhumation. It is difficult to constrain the timing of S0, but it likely occurred between 120

and 90 Ma (Fig. 14). The partially to completely serpentinized peridotite then underwent brecciation. This was likely controlled by chemically induced fracturing and hydro-fracturing, resulting in precipitation of massive serpentine $S1_{all}$. This massive serpentine was then partially to completely carbonated at low temperature. Based on the presence of amphibolite within the breccia, this carbonation likely happened after 90 Ma. Finally, during the shortening event and the subsidence of the Sivas foreland Basin (55−40 Ma), the ophiolites underwent low-temperature carbonation C3. A high-temperature carbonation event C4 followed, and then a final serpentinization event S2 led to the formation of massive serpentine. The youngest episodes in the Eocene could have been associated with oxidizing alteration that led to the formation of hematite associated with calcite C5. We note that it remains unclear whether maghemite formed during seafloor alteration or during incomplete hematitization. Finally, late goethitization could have occurred during meteoric alteration.

5.5 H_2 production and potential:

During serpentinization, H_2 is produced *via* water–rock interaction coupled with oxidation of Fe^{2+} into Fe^{3+} (Klein *et al.*, 2009; Andreani *et al.*, 2013). This means that all minerals containing Fe^{3+} (magnetite, hematite, maghemite, goethite, and serpentine) with variable Fe^{3+}/Fe_{tot} ratios are commonly associated with the production of H_2. It would imply that the higher the Fe^{3+}/Fe_{tot} ratio (in serpentine or bulk), the more H_2 would be likely produced. However, this can only be true if the alteration proceeds in an open-system where H_2 can escape, so that the rock could be oxidized even forming hematite while H_2 is produced and goes out of the system (Klein *et al.*, 2013).

In Sivas ophiolite, Fe^{3+} is present in serpentine, magnetite, maghemite, hematite and goethite. Among these minerals, only the serpentine can have different Fe^{3+}/Fe_{tot} ratios. The different serpentines of the mesh have Fe^{3+}/Fe_{tot} ratio between 0.49 ± 0.08 (2σ) and 0.68 ± 0.14 (2σ). The serpentinites for which nearly 50% of the iron is ferric corresponds to the most pristine zone. This is a value similar than the one measured by Klein *et al.* (2009) whereas the other serpentines of the mesh have higher ferric iron which could be related to a higher H_2 production. According to Andreani *et al.* (2013), any increase in Fe^{3+}/Fe_{tot} ratio implies an increase in the degree of serpentinization. Even if serpentinization is complete in all samples, we propose that higher Fe^{3+}/Fe_{tot} ratios imply more alteration episodes and therefore greater H_2 production. We can note that for most of the rocks, the Fe^{3+}/Fe_{tot} ratio of serpentine is similar than the bulk Fe^{3+}/Fe_{tot} ratio. This would suggest that oxidation state of serpentine represents the oxidation state of the rock.

For the most oxidized rocks, the hematite contains most of the ferric iron and the serpentine does not have the same Fe^{3+}/Fe_{tot} ratio than the bulk rock. Therefore, during the event of hematitization, the serpentine would not have been affected. In this context, H_2 could only have been produced by hematite (Frost, 1985), maybe by the oxidation of magnetite, if H_2 was then lost during the process as discussed previously. In contrast, the veins of serpentine S1' and S2 have a low Fe^{3+}/Fe_{tot} ratio (~0.31). It is unclear whether this lower ratio relates to a more reducing environment or if it reflects higher solubility of Fe^{2+} compared to Fe^{3+} in fluid solutions before the precipitation of serpentine.

We suppose that H_2 produced during the classic serpentinization stage was lost by degassing in the Neo-Tethys ocean as it happens today along all the MOR (Worman *et al.*, 2020). It remains unclear, however, whether H_2 produced by the precipitation of hematite and goethite and during late serpentinization was trapped as a free gas phase. If this H_2 generation still occurred after salt precipitation, some of the H_2 could have been trapped beneath this salt cap or water rich clay levels, if not recombined into CH_4 or consumed by any abiotic or biologic sink (Zgonnik, 2020).

Today, serpentinization can still occur by the alteration of chromite that contains Fe^{2+}, or by the alteration of olivine if it is present in deep peridotite and kinetically possible. No evidence of ongoing alteration has been observed to date.

6 Conclusions

We investigated carbonated ophicalcites from the Sivas ophiolite in order to identify different episodes of alteration, especially an early and a late serpentinization, intercalated with several carbonation events. The first episode of alteration occurred on the seafloor and is characterized by a complete serpentinization of olivine and pyroxene, forming serpentine and magnetite. This was followed by brecciation of the serpentinites, likely occurring in a fault damage zone. The space created during brecciation was filled by massive serpentine. This is one of the first occurrences of massive serpentine present in some fractures. It is not clear if the fracturing was caused by brittle deformation into the damage zone of the fault or by serpentinization-induced fracturing (Renard, 2021). We observed no continuum between serpentinization and carbonation. During cooling related to the exhumation of serpentinized peridotites, seafloor alteration led to low-temperature carbonation after 90 Ma. Finally, we found a reheating of the system that led to a late serpentinization episode, likely during the early Eocene. This is of particular interest because it implies serpentinization associated with the formation of salt deposits at 55−40 Ma (Debure *et al.*, 2019).

H_2 could have been produced during two main alteration events: the first is linked with seafloor exhumation of the Sivas ophiolite, and the second likely took place after obduction. It is thus proposed that the Sivas ophiolite, and likely obducted ophiolites in general, can be a source of H_2 in at least two pulses: one occurring on the seafloor and the other within the continent. This late serpentinization, characterized by massive serpentine crosscutting type II ophicalcite, shows that deep or partially fresh peridotites could still be present and that ongoing serpentinization could be possible. This could result in ongoing H_2 generation, similar to that observed in the Chimaera seeps (Etiope *et al.*, 2011) or in Tuscany (Leila *et al.*, 2021).

In this study, we have shown important features of the Sivas ophiolite that could help better understand the complete alteration process from the seafloor to the continent. Dating measurements also constrain the chronology, particularly for the final stage of serpentinization. Further studies will be

necessary in order to confirm if large quantity of H_2 were trapped under salt deposits, and whether this H_2 can be produced.

Supplementary material

Fig. S1. Mössbauer spectra of (a) B2* zone 1 and (b) D1* and the associated tables with the Mössbauer hyperfine parameters and the different contents of each sub-spectra. The values in brackets denote the error corresponding to the associated value. hem: hematite, mgt: magnetite, spt: serpentine. obs.: observed, calc.: calculated.
Table S1. Serpentine electron microprobe analyses (wt% and number of cations). The detection limits were 640 ppm, 510 ppm, 420 ppm, 640 ppm, 730 ppm, 970 ppm, 1010 ppm, 6760 ppm, 440 ppm, 280 ppm, 930 ppm, 920 ppm, 330 ppm, and 1100 ppm for Na, Si, Al, K, Ca, Mn, Fe, F, Mg, Cl, Ba, Ti, Cr, and Ni, respectively.
Table S2. Calcite electron microprobe analyses (wt% and number of cations). The complement of the total (wt%) is equivalent to CO_2 (wt%). The detection limits were 760 ppm, 400 ppm, 370 ppm, 560 ppm, 1060 ppm, 1010 ppm, 1050 ppm, 10,210 ppm, 450 ppm, 250 ppm, 1010 ppm, 1020 ppm, 350 ppm, and 1130 ppm for Na, Si, Al, K, Ca, Mn, Fe, F, Mg, Cl, Ba, Ti, Cr, and Ni, respectively.

The Supplementary Material is available at https://www.bsgf.fr/10.1051/bsgf/2022015/olm.

Acknowledgments. We thank Johan Villeneuve and Nordine Bouden for their contribution in the SIMS analyses, and Etienne Legeay, Guilhem Hoareau, Mahmoud Lotfy, and Stephen Centrella for constructive discussions. We would like to thank the editor and the reviewers for their constructive criticism of an early version of the paper. This work was supported by Institut Carnot Isifor, and structural geology chair Total UPPA. We thank Isotope Editing for editing the draft of this manuscript.

References

Abrajano TA, Sturchio NC, Bohlke JK, Lyon GL, Poreda RJ, Stevens CM. 1988. Methane-hydrogen gas seeps, Zambales Ophiolite, Philippines: deep or shallow origin? *Chemical Geology* 71: 211–222. https://doi.org/10.1016/0009-2541(88)90116-7.

Abrajano TA, Sturchio NC, Kennedy BM, Lyon GL, Muehlenbachs K, Bohlke JK. 1990. Geochemistry of reduced gas related to serpentinization of the Zambales ophiolite, Philippines. *Applied Geochemistry* 5: 625–630. https://doi.org/10.1016/0883-2927(90)90060-I.

Aktïmur HT, Tekïrlï ME, Yurdakul ME. 1990. Geology of the Sivas-Erzincan Tertiary basin. *Bulletin of the Mineral Research and Exploration Institute of Turkey, Ankara* 111: 21–30.

Allen DE, Seyfried WE. 2003. Compositional controls on vent fluids from ultramafic-hosted hydrothermal systems at mid-ocean ridges: an experimental study at 400 °C, 500 bars. *Geochimica et Cosmochimica Acta* 67: 1531–1542. https://doi.org/10.1016/S0016-7037(02)01173-0.

Andreani M, Muñoz M, Marcaillou C, Delacour A. 2013. μXANES study of iron redox state in serpentine during oceanic serpentinization. *Lithos* 178: 70–83. https://doi.org/10.1016/j.lithos.2013.04.008.

Andreani M, Escartin J, Delacour A, Ildefonse B, Godard M, Dyment J, *et al.* 2014. Tectonic structure, lithology, and hydrothermal signature of the Rainbow massif (Mid-Atlantic Ridge 36°14′N). *Geochem. Geophys. Geosyst.* 15: 3543–3571. https://doi.org/10.1002/2014GC005269.

Artemyev DA, Zaykov VV. 2010. The types and genesis of ophicalcites in Lower Devonian olistostromes at cobalt-bearing massive sulfide deposits in the West Magnitogorsk paleoisland arc (*South Urals*). *Russian Geology and Geophysics* 51: 750–763. https://doi.org/10.1016/j.rgg.2010.06.003.

Bach W, Garrido CJ, Paulick H, Harvey J, Rosner M. 2004. Seawater-peridotite interactions: first insights from ODP Leg 209, MAR 15°N. *Geochemistry, Geophysics, Geosystems* 5. https://doi.org/10.1029/2004GC000744.

Bach W, Paulick H, Garrido CJ, Ildefonse B, Meurer WP, Humphris SE. 2006. Unraveling the sequence of serpentinization reactions: petrography, mineral chemistry, and petrophysics of serpentinites from MAR 15°N (ODP Leg 209, Site 1274). *Geophys Res Lett* 33: L13306. https://doi.org/10.1029/2006GL025681.

Barnes I, Lamarche VC, Himmelberg G. 1967. Geochemical evidence of present-day serpentinization. *Science* 156: 830–832. https://doi.org/10.1126/science.156.3776.830.

Bernoulli D, Weissert H. 2021. Oxygen isotopes in ophicalcites: an ever-lasting controversy? *Int J Earth Sci (Geol Rundsch)* 110: 1–8. https://doi.org/10.1007/s00531-020-01934-5.

Bruni J, Canepa M, Chiodini G, Cioni R, Cipolli F, Longinelli A, *et al.* 2002. Irreversible water-rock mass transfer accompanying the generation of the neutral, Mg-HCO_3 and high-pH, Ca-OH spring waters of the Genova province, Italy. *Applied Geochemistry* 17: 455–474. https://doi.org/10.1016/S0883-2927(01)00113-5.

Callot J-P., Ribes C, Kergaravat C, Bonnel C, Temiz H, Poisson A, *et al.* 2014. Salt tectonics in the Sivas basin (Turkey): crossing salt walls and minibasins. *Bulletin de la Société géologique de France* 185: 33–42. https://doi.org/10.2113/gssgfbull.185.1.33.

Cannat M, Fontaine F, Escartín J. 2010. Serpentinization and associated hydrogen and methane fluxes at slow spreading ridges. In: Rona PA, Devey CW, Dyment J, Murton BJ, eds. Geophysical Monograph Series. Washington, D.C.: American Geophysical Union, pp. 241–264. https://doi.org/10.1029/2008GM000760.

Cardace D, Meyer-Dombard DR, Woycheese KM, Arcilla CA. 2015. Feasible metabolisms in high pH springs of the Philippines. *Front Microbiol* 6 https://doi.org/10.3389/fmicb.2015.00010.

Charlou JL, Donval JP, Fouquet Y, Jean-Baptiste P, Holm N. 2002. Geochemistry of high H2 and CH4 vent fluids issuing from ultramafic rocks at the Rainbow hydrothermal field (36°14′N, MAR). *Chemical Geology* 191: 345–359. https://doi.org/10.1016/S0009-2541(02)00134-1.

Chavagnac V, Monnin C, Ceuleneer G, Boulart C, Hoareau G. 2013. Characterization of hyperalkaline fluids produced by low-temperature serpentinization of mantle peridotites in the Oman and Ligurian ophiolites. *Geochemistry, Geophysics, Geosystems* 14: 2496–2522. https://doi.org/10.1002/ggge.20147.

Cipolli F, Gambardella B, Marini L, Ottonello G, Vetuschi Zuccolini M. 2004. Geochemistry of high-pH waters from serpentinites of the Gruppo di Voltri (Genova, Italy) and reaction path modeling of CO2 sequestration in serpentinite aquifers. *Applied Geochemistry* 19: 787–802. https://doi.org/10.1016/j.apgeochem.2003.10.007.

Coltat R, Boulvais P, Branquet Y, Collot J, Epin ME, Manatschal G. 2019. Syntectonic carbonation during syn-magmatic mantle exhumation at an ocean-continent transition. *Geology* 47: 183–186. https://doi.org/10.1130/G45530.1.

Coltat R, Branquet Y, Gautier P, Boulvais P, Manatschal G. 2020. The nature of the interface between basalts and serpentinized mantle in oceanic domains: Insights from a geological section in the Alps. *Tectonophysics* 228646. https://doi.org/10.1016/j.tecto.2020.228646.

Combaudon V, Moretti I, Kleine BI, Stefánsson A. 2022. Hydrogen emissions from hydrothermal fields in Iceland and comparison with the Mid-Atlantic Ridge. *International Journal of Hydrogen Energy* 47: 10217–10227. https://doi.org/10.1016/j.ijhydene.2022.01.101.

D'Antonio M, Kristensen MB. 2004. Serpentine and brucite of ultramafic clasts from the South Chamorro Seamount (Ocean Drilling Program Leg 195, Site 1200): inferences for the serpentinization of the Mariana forearc mantle. *Mineral Mag* 68: 887–904. https://doi.org/10.1180/0026461046860229.

Darin MH, Umhoefer PJ, Thomson SN. 2018. Rapid Late Eocene exhumation of the Sivas Basin (Central Anatolia) driven by Initial Arabia-Eurasia collision. *Tectonics* 37: 3805–3833. https://doi.org/10.1029/2017TC004954.

Debure M, Lassin A, Marty NC, Claret F, Virgone A, Calassou S, Gaucher EC. 2019. Thermodynamic evidence of giant salt deposit formation by serpentinization: an alternative mechanism to solar evaporation. *Sci Rep* 9: 11720. https://doi.org/10.1038/s41598-019-48138-9.

Deville E, Prinzhofer A. 2016. The origin of N2-H2-CH4-rich natural gas seepages in ophiolitic context: a major and noble gases study of fluid seepages in New Caledonia. *Chemical Geology* 440: 139–147. https://doi.org/10.1016/j.chemgeo.2016.06.011.

Deville EP, Prinzhofer A, Pillot D, Vacquand C, Sissmann O. 2010. Peridote-water interaction generating migration pathways of H2-rich fluids in subduction context: common processes in the ophiolites of Oman, New-Caledonia, Philippines and Turkey. *AGU Fall Meeting Abstracts* 13: T13A–T2184.

Etiope G, Schoell M, Hosgörmez H. 2011. Abiotic methane flux from the Chimaera seep and Tekirova ophiolites (Turkey): understanding gas exhalation from low temperature serpentinization and implications for Mars. *Earth and Planetary Science Letters* 310: 96–104. https://doi.org/10.1016/j.epsl.2011.08.001.

Etiope G, Tsikouras B, Kordella S, Ifandi E, Christodoulou D, Papatheodorou G. 2013. Methane flux and origin in the Othrys ophiolite hyperalkaline springs, Greece. *Chemical Geology* 347: 161–174. https://doi.org/10.1016/j.chemgeo.2013.04.003.

Frost BR. 1985. On the Stability of Sulfides, Oxides, and Native Metals in Serpentinite. *J Petrol* 26: 31–63. https://doi.org/10.1093/petrology/26.1.31.

Frost BR, Beard JS. 2007. On Silica Activity and Serpentinization. *Journal of Petrology* 48: 1351–1368. https://doi.org/10.1093/petrology/egm021.

Frost BR, Evans KA, Swapp SM, Beard JS, Mothersole FE. 2013. The process of serpentinization in dunite from New Caledonia. *Lithos, Serpentinites from mid-oceanic ridges to subduction* 178: 24–39. https://doi.org/10.1016/j.lithos.2013.02.002.

Gaucher EC. 2020. New Perspectives in the Industrial Exploration for Native Hydrogen. *Elements* 16: 8–9. https://doi.org/10.2138/gselements.16.1.8.

Hopkinson LJ, Dee S, Boulter CA. 2000. Moving reactive interfaces and fractal carbonate replacement patterns in serpentinites: evidence from the southern Iberia Abyssal Plain. *Mineral Mag* 64: 791–800. https://doi.org/10.1180/002646100549797.

Hosgormez H, Etiope G, Yalçin MN. 2008. New evidence for a mixed inorganic and organic origin of the Olympic Chimaera fire (Turkey): a large onshore seepage of abiogenic gas. *Geofluids* 8: 263–273. https://doi.org/10.1111/j.1468-8123.2008.00226.x.

İnan S, İnan N. 1990. The features of Gürlevik limestone and a newly suggested name in Tecer formation. *Bulletin of Turkish Geological Society* 15: 406–417.

Kavak KS, Parlak O, Temiz H. 2017. Geochemical characteristics of ophiolitic rocks from the southern margin of the Sivas basin and their implications for the Inner Tauride Ocean, Central-Eastern Turkey. *Geodinamica Acta* 29: 160–180. https://doi.org/10.1080/09853111.2017.1359773.

Kergaravat C, Ribes C, Callot J-P., Ringenbach J-C. 2017. Tectono-stratigraphic evolution of salt-controlled minibasins in a fold and thrust belt, the Oligo-Miocene central Sivas Basin. *Journal of Structural Geology* 102: 75–97. https://doi.org/10.1016/j.jsg.2017.07.007.

Kergaravat C, Ribes C, Legeay E, Callot J-P., Kavak KS, Ringenbach J-C. 2016. Minibasins and salt canopy in foreland fold-and-thrust belts: The central Sivas Basin, Turkey. *Tectonics* 35: 1342–1366. https://doi.org/10.1002/2016TC004186.

Kim S-T., O'Neil JR. 1997. Equilibrium and nonequilibrium oxygen isotope effects in synthetic carbonates. *Geochimica et Cosmochimica Acta* 61: 3461–3475. https://doi.org/10.1016/S0016-7037(97)00169-5.

Klein F, Bach W, Humphris SE, Kahl W-A., Jöns N, Moskowitz B, *et al.* 2014. Magnetite in seafloor serpentinite—Some like it hot. *Geology* 42: 135–138. https://doi.org/10.1130/G35068.1.

Klein F, Bach W, Jöns N, McCollom T, Moskowitz B, Berquó T. 2009. Iron partitioning and hydrogen generation during serpentinization of abyssal peridotites from 15°N on the Mid-Atlantic Ridge. *Geochimica et Cosmochimica Acta* 73: 6868–6893. https://doi.org/10.1016/j.gca.2009.08.021.

Klein F, Bach W, McCollom TM. 2013. Compositional controls on hydrogen generation during serpentinization of ultramafic rocks. *Lithos* 178: 55–69. https://doi.org/10.1016/j.lithos.2013.03.008.

Lafay R, Baumgartner LP, Stephane S, Suzanne P, German M-H., Torsten V. 2017. Petrologic and stable isotopic studies of a fossil hydrothermal system in ultramafic environment (Chenaillet ophicalcites, Western Alps, France): processes of carbonate cementation. *Lithos* 294–295: 319–338. https://doi.org/10.1016/j.lithos.2017.10.006.

Lefebvre C, Barnhoorn A, van Hinsbergen DJJ, Kaymakci N, Vissers RLM. 2011. Late Cretaceous extensional denudation along a marble detachment fault zone in the Kırsehir massif near Kaman, central Turkey. *Journal of Structural Geology* 33: 1220–1236. https://doi.org/10.1016/j.jsg.2011.06.002.

Legeay E. 2017. Géodynamique du Bassin de Sivas (Turquie)—De la fermeture d'un domaine océanique à la mise en place d'un avant-pays salifère. France: UPPA.

Legeay E, Mohn G, Callot J, Ringenbach J, Ulianov A, Kavak KS. 2019. The Pre-Obduction to Post-Obduction Evolution of the Sivas Ophiolite (Turkey) and Implications for the Precollisional History of Eastern Anatolia. *Tectonics* 38: 2114–2141. https://doi.org/10.1029/2018TC005114.

Leila M, Lévy D, Battani A, Piccardi L, Šegvić B, Badurina L, *et al.* 2021. Origin of continuous hydrogen flux in gas manifestations at the Larderello geothermal field, Central Italy. *Chemical Geology* 585: 120564. https://doi.org/10.1016/j.chemgeo.2021.120564.

Lemoine M, Tricart P, Boillot G. 1987. Ultramafic and gabbroic ocean floor of the Ligurian Tethys (Alps, Corsica, Apennines): In search of a genetic model. *Geol.* 15: 622. https://doi.org/10.1130/0091-7613(1987)15<622:UAGOFO>2.0.CO;2.

Manatschal G, Froitzheim N, Rubenach M, Turrin BD. 2001. The role of detachment faulting in the formation of an ocean-continent transition: insights from the Iberia Abyssal Plain. *Geological*

Society, London, Special Publications 187: 405–428. https://doi.org/10.1144/GSL.SP2001.187.01.20.

McCollom TM, Seewald JS. 2007. Abiotic Synthesis of Organic Compounds in Deep-Sea Hydrothermal Environments. *Chem Rev* 107: 382–401. https://doi.org/10.1021/cr0503660.

Meyer-Dombard DR, Woycheese KM, Yargıçoğlu EN, Cardace D, Shock EL, Güleçal-Pektas Y, *et al.* 2015. High pH microbial ecosystems in a newly discovered, ephemeral, serpentinizing fluid seep at Yanartas (Chimera), Turkey. *Front Microbiol* 5. https://doi.org/10.3389/fmicb.2014.00723.

Moody JB. 1976. Serpentinization: a review. *Lithos* 9: 125–138. https://doi.org/10.1016/0024-4937(76)90030-X.

Moretti I. 2019. H2: energy vector or source? *L'Actualité chimique*.

Neal C, Stanger G. 1983. Hydrogen generation from mantle source rocks in Oman. *Earth and Planetary Science Letters* 66: 315–320. https://doi.org/10.1016/0012-821X(83)90144-9.

Noël J. 2019. Étude pétro-structurale et géochimique des processus de serpentinisation et de carbonatation des péridotites de l'ophiolite d'Oman, dissertation.

O'Hanley DS. 1992. Solution to the volume problem in serpentinization. *Geology* 20: 705–708. https://doi.org/10.1130/0091-7613(1992)020<0705:STTVPI>2.3.CO;2.

Oufi O, Cannar M, Horen H. 2002. Magnetic properties of variably serpentinized abyssal peridotites. *J Geophys Res* 107: 2095. https://doi.org/10.1029/2001JB000549.

Parlak O. 2016. The tauride ophiolites of Anatolia (Turkey): a review. *J Earth Sci* 27: 901–934. https://doi.org/10.1007/s12583-016-0679-3.

Paulick H, Bach W, Godard M, De Hoog JCM, Suhr G, Harvey J. 2006. Geochemistry of abyssal peridotites (Mid-Atlantic Ridge, 15°20′N, ODP Leg 209): implications for fluid/rock interaction in slow spreading environments. *Chemical Geology* 234: 179–210. https://doi.org/10.1016/j.chemgeo.2006.04.011.

Picazo S, Malvoisin B, Baumgartner L, Bouvier A-S. 2020. Low Temperature Serpentinite Replacement by Carbonates during Seawater Influx in the Newfoundland Margin. *Minerals* 10: 184. https://doi.org/10.3390/min10020184.

Pichat A. 2017. Dynamique des systèmes évaporitiques d'un bassin d'avant-pays salifère et processus diagénétiques associés au contexte halocinétique : exemple du bassin de Sivas en Turquie. France: UPPA.

Pichat A, Hoareau G, Callot J-P., Legeay E, Kavak KS, Révillon S, *et al.* 2018. Evidence of multiple evaporite recycling processes in a salt-tectonic context, Sivas Basin, Turkey. *Terra Nova* 30: 40–49. https://doi.org/10.1111/ter.12306.

Pichat A, Hoareau G, Lopez M, Callot J-P., Ringenbach J-C. 2021. Sedimentology and depositional environment of the Late Eocene marine siliciclastic to evaporite transition in the Sivas Basin (Turkey). *Marine and Petroleum Geology* 131: 105151. https://doi.org/10.1016/j.marpetgeo.2021.105151.

Pucéat E, Lécuyer C, Sheppard SMF, Dromart G, Reboulet S, Grandjean P. 2003. Thermal evolution of Cretaceous Tethyan marine waters inferred from oxygen isotope composition of fish tooth enamels. *Paleoceanography* 18. https://doi.org/10.1029/2002PA000823.

Renard F. 2021. Reaction-induced fracturing: when chemistry breaks rocks. *J Geophys Res Solid Earth* 126. https://doi.org/10.1029/2020JB021451.

Ribes C. 2015. Interaction entre la tectonique salifère et la sédimentation dans des mini-bassins : exemple de l'Oligo-Miocène du bassin de Sivas, Turquie. France: UPPA.

Ribes C, Kergaravat C, Bonnel C, Crumeyrolle P, Callot J-P., Poisson A, *et al.* 2015. Fluvial sedimentation in a salt-controlled mini-basin: stratal patterns and facies assemblages, Sivas Basin, Turkey. *Sedimentology* 62: 1513–1545. https://doi.org/10.1111/sed.12195.

Ribes C, Lopez M, Kergaravat C, Crumeyrolle P, Poisson A, Callot J-P, *et al.* 2018. Facies partitioning and stratal pattern in salt-controlled marine to continental mini-basins: examples from the Late Oligocene to Early Miocene of the Sivas Basin, Turkey. *Marine and Petroleum Geology* 93: 468–496. https://doi.org/10.1016/j.marpetgeo.2018.03.018.

Ringenbach J-C., Salel J-F., Kergaravat C, Ribes C, Bonnel C, Callot J-P. 2013. Salt tectonics in the Sivas Basin, Turkey: outstanding seismic analogues from outcrops. *First Break* 31. https://doi.org/10.3997/1365-2397.2013016.

Rouméjon S, Cannat M. 2014. Serpentinization of mantle-derived peridotites at mid-ocean ridges: mesh texture development in the context of tectonic exhumation. *Geochem Geophys Geosyst* 15: 2354–2379. https://doi.org/10.1002/2013GC005148.

Rouméjon S, Cannat M, Agrinier P, Godard M, Andreani M. 2015. Serpentinization and Fluid Pathways in Tectonically Exhumed Peridotites from the Southwest Indian Ridge (62–65°E). *J Petrol* 56: 703–734. https://doi.org/10.1093/petrology/egv014.

Sano Y, Urabe A, Wakita H, Wushiki H. 1993. Origin of hydrogen-nitrogen gas seeps, Oman. *Applied Geochemistry* 8: 1–8. https://doi.org/10.1016/0883-2927(93)90053-J.

Schrenk MO, Brazelton WJ, Lang SQ. 2013. Serpentinization, Carbon, and Deep Life. *Reviews in Mineralogy and Geochemistry* 75: 575–606. https://doi.org/10.2138/rmg.2013.75.18.

Schwartz S, Guillot S, Reynard B, Lafay R, Debret B, Nicollet C, *et al.* 2013. Pressure-temperature estimates of the lizardite/antigorite transition in high pressure serpentinites. *Lithos* 178: 197–210. https://doi.org/10.1016/j.lithos.2012.11.023.

Schwarzenbach EM, Früh-Green GL, Bernasconi SM, Alt JC, Plas A. 2013. Serpentinization and carbon sequestration: A study of two ancient peridotite-hosted hydrothermal systems. *Chemical Geology* 351: 115–133. https://doi.org/10.1016/j.chemgeo.2013.05.016.

Seyfried WE, Foustoukos DI, Fu Q. 2007. Redox evolution and mass transfer during serpentinization: an experimental and theoretical study at 200 °C, 500bar with implications for ultramafic-hosted hydrothermal systems at Mid-Ocean Ridges. *Geochimica et Cosmochimica Acta* 71: 3872–3886. https://doi.org/10.1016/j.gca.2007.05.015.

Szponar N, Brazelton WJ, Schrenk MO, Bower DM, Steele A, Morrill PL. 2013. Geochemistry of a continental site of serpentinization, the Tablelands Ophiolite, Gros Morne National Park: A Mars analogue. *Icarus, Terrestrial Analogs for Mars: Mars Science Laboratory and Beyond* 224: 286–296. https://doi.org/10.1016/j.icarus.2012.07.004.

Taber S. 1916. The growth of Crystals under external pressure. *Growth of Crystals* 532–556.

Vacquand C, Deville E, Beaumont V, Guyot F, Sissmann O, Pillot D, *et al.* 2018. Reduced gas seepages in ophiolitic complexes: evidences for multiple origins of the H2-CH4-N2 gas mixtures. *Geochimica et Cosmochimica Acta* 223: 437–461. https://doi.org/10.1016/j.gca.2017.12.018.

van Hinsbergen DJJ, Maffione M, Plunder A, Kaymakcı N, Ganerød M, Hendriks BWH, *et al.* 2016. Tectonic evolution and paleogeography of the Kırsehir Block and the Central Anatolian Ophiolites, Turkey. *Tectonics* 35: 983–1014. https://doi.org/10.1002/2015TC004018.

Veizer J, Prokoph A. 2015. Temperatures and oxygen isotopic composition of Phanerozoic oceans. *Earth-Science Reviews* 146: 92–104. https://doi.org/10.1016/j.earscirev.2015.03.008.

Warren JK. 2016. Evaporites: a Geological Compendium. Springer.

White WM. 2015. Isotope Geochemistry. Wiley.
Wiltschko DV, Morse JW. 2001. Crystallization pressure versus "crack seal" as the mechanism for banded veins 4.
Worman SL, Pratson LF, Karson JA, Schlesinger WH. 2020. Abiotic hydrogen (H2) sources and sinks near the Mid-Ocean Ridge (MOR) with implications for the subseafloor biosphere. *PNAS* 117: 13283–13293.. https://doi.org/10.1073/pnas.2002619117.
Woycheese KM, Meyer-Dombard DR, Cardace D, Argayosa AM, Arcilla CA. 2015. Out of the dark: transitional subsurface-to-surface microbial diversity in a terrestrial serpentinizing seep (Manleluag, Pangasinan, the Philippines). *Front Microbiol* 6 https://doi.org/10.3389/fmicb.2015.00044.
Yaliniz MK, Göncüoğlu MC, Özkan-Altiner S. 2000. Formation and emplacement ages of the SSZ-type Neotethyan ophiolites in Central Anatolia, Turkey: palaeotectonic implications. *Geological Journal* 35: 53–68. https://doi.org/10.1002/1099-1034(200004/06)35:2<53::AID-GJ837>3.0.CO;2-6.
Zgonnik V. 2020. The occurrence and geoscience of natural hydrogen: a comprehensive review. *Earth-Science Reviews* 203: 103140. https://doi.org/10.1016/j.earscirev.2020.103140.

Cite this article as: Lévy D, Callot J-P, Moretti I, Duttine M, Dubreuil B, de Parseval P, Boudouma O. 2022. Successive phases of serpentinization and carbonation recorded in the Sivas ophiolite (Turkey), from oceanic crust accretion to post-obduction alteration, *BSGF - Earth Sciences Bulletin* 193: 12.